PHYSICAL REVIEW E **83**, 061605 (2011)

Global stabilities, selection of steady cellular growth, and origin of side branches in directional solidification

Jian-Jun Xu[*]

Department of Mathematics and Statistics, McGill University, Montreal, Quebec, Canada H3A 2K6,
School of Material Science and Engineering, University of Science and Technology in Beijing, Beijing 100083, China,
School of Mathematical Science, Nankai University, Tianjin 300071, China

Yong-Qiang Chen[†]

Department of Fundamental Subject, Tianjin Institute of Urban Construction, Tianjin 300384, China,
School of Mathematical Science, Nankai University, Tianjin 300071, China

(Received 26 January 2011; published 28 June 2011)

The present paper investigates the global instability mechanisms of arrayed-cellular growth with asymptotic approach. We find that the system of directional solidification involves two types of global instability mechanisms: the low-frequency instability and the global oscillatory instability, which are profoundly similar to that found in the system of viscous fingering and free dendritic growth. Based on these global instabilities, the neutral mode selection principle for the limiting state of growth is proposed; the origin and essence of side branching on the interface are elucidated with the so-called global trapped wave mechanism, which involves the interfacial wave reflection and amplification along the interface. It is demonstrated that side branching is self-sustaining and can persist without continuously applying the external noise; the effect of the anisotropy of interfacial energy is not essential for the selection of steady cellular growth and for the origin and formation of side branching at the interface. The comparisons of theoretical results are made with the most recent experimental works and the numerical simulations which show very good quantitative agreement.

DOI: 10.1103/PhysRevE.83.061605 PACS number(s): 81.10.Aj, 81.30.Fb, 05.65.+b, 47.54.−r

I. INTRODUCTION

Deep arrayed-cellular and dendritic pattern formation during solidification is one of the fundamental subjects in material science [1–27]. It is also a typical pattern-formation phenomenon investigated in nonlinear science. The formation of arrayed-cellular patterns in a solidifying system of binary alloy can be well observed in a Hele-Shaw cell as sketched in Fig. 1.

The system consists of a thin sample material and two uniform temperature zones: a hot zone with a temperature higher than the melting temperature of a flat interface and a cold zone with a temperature lower than the melting temperature. The sample is pulled at a constant velocity V along the direction from the hot zone to the cold zone. Experimental results show that when the pulling velocity V is sufficiently small, the interface will be flat, located somewhere between the two zones. When the pulling velocity increases beyond a critical number V_c, the flat interface becomes unstable due to the Mullins-Sekerka instability (see Refs. [2,3]). Beyond V_c, the interface will continuously evolve, and after a complicated dynamical process, it eventually forms a steady arrayed-cellular structure with the tip located at, say, $y = 0$. These cells are aligned periodically with equal primary spacing ℓ_w and the relative width of cell λ_0 defined as the ratio of the asymptotic width of the cell and ℓ_w (see Fig. 2). It is further observed that when the pulling velocity is larger than a second critical number, the cellular array transforms to a dendritic array. The basic issues for the above phenomenon include the following: what is a limiting steady state of arrayed-cellular growth as the time $t \to \infty$, whether the selected limiting state is unique or not, what is the stability property of the steady state, what is the origin and essence of the side branching appearing on the interface, and what is the mechanism for the transition from cellular array to dendritic array?

The subject has been studied analytically for a long time by a number authors (see Refs. [11–19]). For instance, in 1985 Pelcé and Pumir studied the steady state of cellular growth [4] for the isothermal case; in 1986 Dombre and Haankim investigated the case $\lambda_0 \approx 1$ [6]; later Karma and Pelcé worked on the stability of deep cellular growth analytically [7–11], and Losert *et al.* investigated the stability mechanisms and formation of doublets using numerical simulations [12]. In addition to these authors, this subject has also been analytically investigated by Weeks and van Saarloons, Grant [13,15], Davis [16,18], Caroli *et al.* [17], Billia and Trivedi [19], and others. However, all the previous analytical works have not found the linear instability mechanisms of the system with the relevant expressions of global solutions or the corresponding quantization conditions and the features of neutral curves, or have provided the selection conditions for the cellular array and dendritic array formation at a later stage of growth.

In recent years, Pocheau *et al.* performed a sequence of experimental measurements on the dynamics of arrayed-cellular pattern formation in the Hele-Shaw cell, as well as the global interface shapes under various growth conditions (see Refs. [25–27]). Their experimental data show that under given growth conditions the selected arrayed-cellular pattern is not unique; it depends on the history of growth. Their data and results are in need of theoretical interpretations. The subject has also been studied by many researchers numerically with the phase field model in recent years (see, for instance,

---

[*] jianjun_xu@nankai.edu.cn
[†] yonqiang@gmail.com

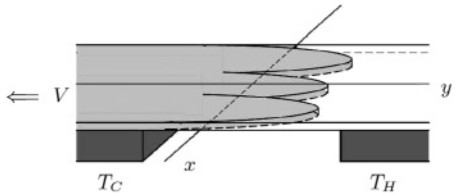

FIG. 1. Sketch of a directional solidification device, Hele-Shaw cell.

Refs. [28–30]). The numerical simulations may reproduce the cellular patterns resembling those observed in the experiments. However, these works do not offer further understanding of the relevant physical instability mechanisms. For instance, the results given in Ref. [30] revealed the numerical phenomena, that during the arrayed-dendritic growth the frequency of oscillation at the interface was a constant independent of the distance behind the tip, and the power spectrum of the interfacial oscillation contained a sequence of peaks with progressively decreasing heights. The numerical simulations cannot give answers to the questions associated with the intrinsic essence and mechanisms of these phenomena, such as what is the nature of the constant frequency observed, are there special physical implications of these peaks and the distances between each peak from others in the power spectrum obtained, and are there any intrinsic connections between all these data? If the answers are yes, what are they?

Therefore, the key issues of the subject still remain unresolved.

It is evident that the understanding of stabilities of a system of cellular growth is the critical element for resolving all the issues raised. In the present paper, we attempt to explore analytically the global stability mechanisms of the steady-state solutions for two-dimensional (2D) deep arrayed-cellular growth with isotropic surface tension in a Hele-Shaw cell. On the basis of these results, we hope to resolve the problems given above.

We performed global linear stability analysis for the basic state of cellular growth in the system of curvilinear coordinates based on the Saffmen-Taylor solution for viscous fingering formation (see Refs. [31–37]) and found that the system under study allowed two types of global instability mechanisms: the low-frequency (LF) instability and the global trapped wave (GTW) instability, which were first identified in the interfacial wave (IFW) theory for the system of free dendritic growth [37]. These two stability mechanisms yield two branches of neutral curves: the fingerlike branch, which gives the basic states with a smooth steady or nearly steady arrayed-cellular interface, and the needlelike branch, which yields the basic states with a self-sustaining, oscillatory, arrayed-dendritic interface. It is expected that in the nonlinear regime, the linear neutrally stable GTW modes will eventually evolve to the limit cycles in the state space. Based on these results, we proposed the *neutrally stable mode* (NSM) selection principle for determination of the limiting states of system as time $t \to \infty$. It is, therefore, derived that given the growth conditions and the material properties, what can be selected at the late stage of growth is just the relationship between the tip radius ℓ_t and the primary spacing ℓ_w. In other words, the limiting state and its interface shape is not unique; they may vary, depending on the history of growth. These findings are consistent with the conclusion drawn by Pocheau *et al.* [25] from their experimental results. Quantitative comparisons of theoretical predictions with corresponding experimental data by Georgelin and Pocheau [25,27] are made, and we find that both are in very good agreement.

It is also derived that the origin and essence of the side branching observed in directional solidification is the same as in the system of free single dendritic growth, the existence of a discrete set of oscillatory GTW modes in the system, which are generated by the so-called trapped wave instability mechanism involving the reflections and amplification of interfacial waves. Therefore the side branching observed in directional solidification, which may be described by the

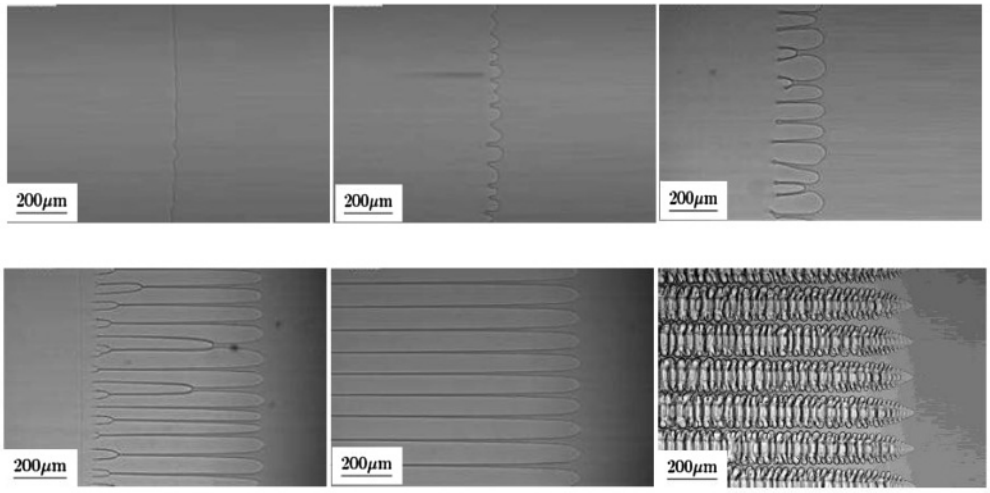

FIG. 2. Typical arrayed cellular and dendritic interface patterns observed in experiments of directional solidification, arranged in the order of increasing pulling speed from left to right and from top to bottom. (Courtesy of W. D. Huang and Xin Lin.)

neutrally stable GTW mode ($n = 0$) combining with the decaying GTW modes ($n = 1,2,\ldots$) at the late stage of growth, is self-sustaining and can persist without the noise continuously added to the system. The theory established in the present paper demonstrates well the physical implications and the nature of the side branching's behaviors, as well as the power spectrum's characteristics explored in the numerical simulations by Echebarria *et al.* [30], as the resonance of the cellular growth system with the small external perturbations with the eigenfrequencies.

The present paper is arranged as follows. In Sec. II we give the mathematical formulation for directional solidification from a binary mixture in terms of the curvilinear coordinate system (ξ,η). In Sec. III we give the basic state solution and the linear perturbation system. In Sec. IV we derive the outer solution for the perturbed states in the outer region by applying the multiple-variable expansion (MVE) method. It is found that the MVE solution has a singularity at the point $\zeta = \zeta_c$ in the extended complex $\zeta = \xi + i\xi_I$ plane. In Sec. V we derive the inner solution in the vicinity of the singular point $(\zeta_c,0)$ in the extended space (ζ,η). Two different cases are investigated separately: the case of a complex spectrum of eigenvalues $\sigma_0 = \sigma_{0,R} - i\omega_0$ with $|\sigma_0| = O(1)$ and the case of a real spectrum of eigenvalues with $|\sigma_0| \ll 1$. In Sec. VI we give the two global instability mechanisms: the global trapped wave (GTW) stability and the low-frequency (LF) stability. Based on these results, the neutrally stable mode (NSM) selection principle of the limiting state of cellular growth is proposed. In Sec. VII we discuss the selection of steady arrayed-cellular growth and compare the theoretical predictions with the experimental data. In Sec. VIII we discuss the selection of oscillatory arrayed-dendritic growth. We demonstrate the origin and essence of the side branching on the basis of the global trapped waves mechanism. In Sec. IX we discuss the transition from the steady cellular array to the dendritic array. Finally in Sec. X, we summarize the results and give conclusions.

II. MATHEMATICAL FORMULATION OF DIRECTIONAL SOLIDIFICATION FROM BINARY MIXTURE

We assume that the temperature near the cell's tip is linear with given gradient $(G)_D$; the minor species in this binary mixture system, considered as an impurity, is dilute; the solute diffusion in the solid phase is negligible; while other thermodynamic properties are the same for both solid and liquid phases and there is no convection in the system. In the present paper we take into account only the isotropic component of the interfacial energy, although there is numerical evidence showing that the anisotropy of interfacial energy plays a significant role in selecting the growth direction and some types of interfacial pattern formation in the system. Our results will show that the effect of the anisotropy of interfacial energy is not essential for the selection of steady arrayed cellular growth and the origin and formation of side branching at the interface.

The solute diffusion length in the system is denoted as $\ell_D = \kappa_D/V$, where κ_D is the solute diffusivity. We use the tip radius ℓ_t as the length scale, the pulling velocity V as the velocity scale, and ℓ_t/V as the time scale. The scales of the temperature T and concentration C are set as $\Delta H/(c_p\rho)$ and C_∞, respectively. Herein, ΔH is latent heat release per unit of volume of the solid phase, c_p is specific heat, ρ is the density of the melt, and C_∞ is the impurity concentration in the far field. In the present system, one may define the following dimensionless parameters: the Péclet number, $\mathrm{Pe} = \ell_t/\ell_D$; the morphological parameter, $\mathbb{M} = -\frac{mC_\infty}{\Delta H/(c_p\rho)}$, where $m < 0$ is the slope of the liquidus in the phase diagram; the interfacial stability parameter, $\varepsilon = \sqrt{\Gamma} = \sqrt{\ell_c/\ell_t}$, where ℓ_c is the capillary length defined as $\ell_c = \gamma c_p \rho T_{M0}/(\Delta H)^2$ and γ is the surface tension coefficient; the dimensionless gradient of the temperature, $G = \frac{\ell_D}{\Delta H/(c_p\rho)}(G)_D$; the ratio of two length scales, $\lambda_G = \ell_D/\ell_G$, where $\ell_G = -mC_\infty/(G)_D$; and the primary spacing parameter, $W = \ell_w/\ell_t$. In the realistic cases, the interfacial stability parameter ε is always very small. Hence, we may use ε as the basic small parameter. Furthermore, the Péclet number is also small and can be written as $\mathrm{Pe} = \varepsilon\hat{\mathrm{Pe}}$, where $\hat{\mathrm{Pe}} = O(1)$.

We adopt the curvilinear coordinate system (ξ,η) based on the Saffmen-Taylor solution for viscous fingering problem (see Refs. [31–37]): $Z = X + iY = Z(\hat{\zeta}) = \lambda_0\hat{\zeta} + i\frac{2(1-\lambda_0)}{\pi}\ln\cos(\frac{\pi\hat{\zeta}}{2})$, where $X = x/W, Y = y/W$, $\xi = -\Psi(X,Y), \eta = \Phi(X,Y), \hat{\zeta} = \xi + i\eta$, and $\Psi(X,Y)$, $\Phi(X,Y)$ are the stream and potential function of Hele-Shaw flow, respectively. The variables $\{\xi = \xi(X,Y); \eta = \eta(X,Y)\}$ constitute a new orthogonal curvilinear coordinate system on the (X,Y) plane as shown in Fig. 3, and we have $x = WX(\xi,\eta), y = WY(\xi,\eta)$. In the curvilinear coordinate system (ξ,η), the linear distribution of temperature field is described by $T(\xi,\eta,\varepsilon) = \varepsilon\hat{\mathrm{Pe}}G[WY(\xi,\eta) - y_0]$.

We assume that the unsteady arrayed-cellular growth solutions are periodic in space. Thus, one may consider only a single cell. In this case the problem is equivalent to the model problem: fingerlike crystal growth in a channel with fixed side walls $x = \pm W$. In the realistic system of arrayed-cellular growth, of course, the width W is the primary spacing of the array, which is unknown *a priori*.

Under the curvilinear coordinate system (ξ,η), the general unsteady cellular growth is subject to the following governing equation:

$$\frac{\partial^2 C}{\partial \xi^2} + \frac{\partial^2 C}{\partial \eta^2} = \varepsilon W\hat{\mathrm{Pe}}\left(\mathcal{G}^2\frac{\partial C}{\partial t} - Y_\xi\frac{\partial C}{\partial \xi} - X_\xi\frac{\partial C}{\partial \eta}\right) \quad (1)$$

and the boundary conditions:

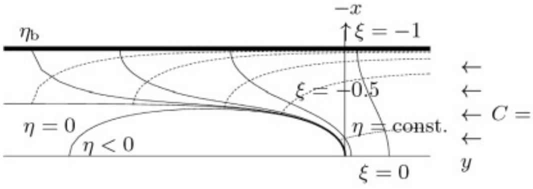

FIG. 3. The sketch of the orthogonal curvilinear coordinate system (ξ,η) based on the ST zero-surface-tension steady-state solutions.

(1) In the far field, as $\eta \to \infty$, $C \to 1$.

(2) At the side walls, $\xi = \pm 1$: $\frac{\partial C}{\partial \xi} = 0$.

(3) At the interface $\eta = \eta_s(\xi,t,\varepsilon)$, (a) the Gibbs-Thomson condition:

$$C = y_* - \varepsilon W\hat{\mathrm{P}}\mathrm{e}\lambda_{\mathrm{G}} Y(\xi,\eta_s) - \frac{\varepsilon^2}{\mathbb{M}W}\mathcal{K}\{\eta_s\},$$

where $\mathcal{K}$ is the twice mean curvature, $y_* = \varepsilon\hat{\mathrm{P}}\mathrm{e}\lambda_{\mathrm{G}} y_0$, and (b) the mass conservation condition:

$$\frac{\partial C}{\partial \eta} - \eta_s' \frac{\partial C}{\partial \xi} + \varepsilon W\hat{\mathrm{P}}\mathrm{e}(1-\kappa)C\left(\mathcal{G}^2\frac{\partial \eta_s}{\partial t} - Y_\xi \eta_s' + Y_\eta\right) = 0,$$

where κ is the segregation coefficient.

In addition to the above boundary conditions, we have the smoothness conditions at the cell's tip and the properly imposed conditions at the bottom of the root.

III. OUTER SOLUTIONS OF LINEAR PERTURBATIONS AROUND THE BASIC STEADY STATE

A. Basic steady-state solutions

In Ref. [33] we have obtained the global solution of steady cellular growth, whose interface shape in a typical case is shown in Fig. 4. This solution contains two free parameters, the tip radius ℓ_t and the primary spacing ℓ_w, and will be used as the basic state in the present paper.

Note that there are differences between the current notation and the notation used in Ref. [33], and the relationships between them are $\varepsilon = \epsilon\sqrt{\hat{\Gamma}}, \hat{\mathrm{P}}\mathrm{e} = 1/\sqrt{\hat{\Gamma}}$. With the current notation, the global steady-state solution has the following global asymptotic expansion form: as $\varepsilon \to 0$,

$$\begin{aligned} C_{\mathrm{B}}(\xi,\eta,\varepsilon) &= [1 + (y_{*0} - 1)\mathrm{e}^{-\varepsilon\hat{\mathrm{P}}\mathrm{e}W\eta}] \\ &\quad + \varepsilon\hat{\mathrm{P}}\mathrm{e}\{y_{*1}\mathrm{e}^{-\varepsilon\hat{\mathrm{P}}\mathrm{e}W\eta} + W\lambda_G[\eta - Y(\xi,\eta)]\} + \cdots, \\ \eta_{\mathrm{B}}(\xi,\varepsilon) &\approx \varepsilon\hat{\mathrm{P}}\mathrm{e}h_1(\xi) + (\text{h.o.t.}), \end{aligned}$$

where $h_1(\xi)$ is the leading approximation of the solution $\eta_{\mathrm{B}}(\xi,\varepsilon)$ and h.o.t. stands for higher-order terms.

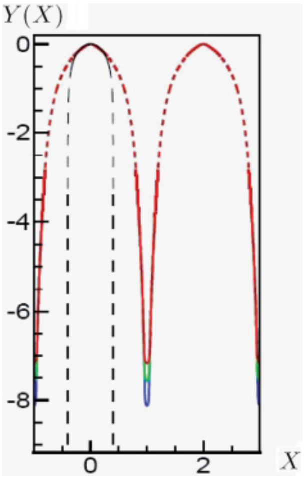

FIG. 4. (Color online) The interface shape of the basis state described on (X,Y) plane for the typical case: $\kappa = 0.1$, $\mathbb{M} = 1.0$, $\lambda_0 = 0.4$, $\lambda_{\mathrm{G}} = 0.8$, and $\hat{\Gamma} = 2.0, 3.0, 4.0$ for the mode $n = 0$ from bottom to top. The black dashed line is given by the Saffman-Taylor solution.

In the subregion near the interface, $\eta = O(1)$, the steady solution can be simplified as

$$\begin{aligned} C_{\mathrm{B}} = y_{*0} + \varepsilon\hat{\mathrm{P}}\mathrm{e}\{&y_{*1} - W\lambda_G Y(\xi,\eta) \\ &+ W[\lambda_{\mathrm{G}} - (y_{*0} - 1)]\eta\} + \cdots, \end{aligned} \tag{2}$$

where $y_{*0} = \frac{1+\lambda_{\mathrm{G}}(1-\lambda_0)}{1-\lambda_0(1-\kappa)}$, $y_{*1} = \frac{W(1-\kappa)\lambda_0\lambda_{\mathrm{G}}\beta_0}{(1-\kappa)\lambda_0-1}$, and $\beta_0 = -\frac{2(1-\lambda_0)}{\pi}\ln 2$. Here $\lambda_0 = \frac{y_{*0}-1-\lambda_{\mathrm{G}}}{(1-\kappa)y_{*0}-\lambda_{\mathrm{G}}}$ is the asymptotic width parameter, which is connected with the primary spacing W via the formula $W = \frac{\pi(1-\lambda_0)}{2\lambda_0^2} + \cdots (\varepsilon \to 0)$.

B. Linear perturbation system

We express the unsteady solutions in two parts:

$$\begin{aligned} C(\xi,\eta,t,\varepsilon) &= C_{\mathrm{B}}(\xi,\eta,\varepsilon) + \tilde{C}(\xi,\eta,t,\varepsilon), \\ \eta_s(\xi,t,\varepsilon) &= \eta_{\mathrm{B}}(\xi,\varepsilon) + \tilde{\eta}_s(\xi,t,\varepsilon). \end{aligned} \tag{3}$$

The first part is the steady basic state, while the second part is the perturbed states. In the present paper, we assume that λ_0 is a given constant; thus, the primary spacing W_0 and cell's tip location y_* are also undisturbed.

By substituting (3) into the above system and linearizing, one may obtain the linear perturbed system, whose coefficients of the perturbation system are functions of variables (ξ,η) depending on the basic state C_{B} and the small parameter ε. Up to the first-order approximation $O(\varepsilon)$ in the subregion near the interface, from (2) we derive the following formulas:

$$\begin{aligned} \frac{\partial C_{\mathrm{B}}}{\partial \eta}(\xi,\eta_{\mathrm{B}},\varepsilon) &\approx \varepsilon W\hat{\mathrm{P}}\mathrm{e}(\lambda_{\mathrm{G}} - y_{*0} + 1) \\ &\quad - \varepsilon W\hat{\mathrm{P}}\mathrm{e}\lambda_G Y_\eta(\xi,0), \\ \frac{\partial^2 C_{\mathrm{B}}}{\partial \eta^2}(\xi,\eta_{\mathrm{B}},\varepsilon) &\approx -\varepsilon W\hat{\mathrm{P}}\mathrm{e}\lambda_G Y_{\eta\eta}(\xi,0), \\ \frac{\partial C_{\mathrm{B}}}{\partial \xi}(\xi,\eta_{\mathrm{B}},\varepsilon) &\approx -\varepsilon W\hat{\mathrm{P}}\mathrm{e}\lambda_G Y_\xi(\xi,0), \\ \frac{\partial^2 C_{\mathrm{B}}}{\partial \xi \partial \eta}(\xi,\eta_{\mathrm{B}},\varepsilon) &\approx -\varepsilon W\hat{\mathrm{P}}\mathrm{e}\lambda_G Y_{\xi\eta}(\xi,0). \end{aligned} \tag{4}$$

The perturbed system can then be written as follows:

$$\frac{\partial^2 \tilde{C}}{\partial \xi^2} + \frac{\partial^2 \tilde{C}}{\partial \eta^2} = \varepsilon W\hat{\mathrm{P}}\mathrm{e}\left(\mathcal{G}^2\frac{\partial \tilde{C}}{\partial t} - Y_\xi\frac{\partial \tilde{C}}{\partial \xi} - X_\xi\frac{\partial \tilde{C}}{\partial \eta}\right) \tag{5}$$

with boundary conditions:

1. In the far field, as $\eta \to \infty$, $\tilde{C} \to 0$
2. At the side walls, $\xi = \pm 1$, $\frac{\partial \tilde{C}}{\partial \xi} = 0$
3. At the interface $\eta = \eta_{\mathrm{B}}$,

$$\begin{aligned} \tilde{C} + \tilde{\eta}_s C_{\mathrm{B},\eta}(\xi,0) = -,\varepsilon W\hat{\mathrm{P}}\mathrm{e}\lambda_{\mathrm{G}} Y_\eta(\xi,0)\tilde{\eta}_s& \\ + \frac{\varepsilon^2}{\mathbb{M}W\mathcal{G}(\xi,0)}\frac{\partial^2 \tilde{\eta}_s}{\partial \xi^2} + (\text{h.o.t.})& \end{aligned} \tag{6}$$

and

$$\begin{aligned} &\frac{\partial \tilde{C}}{\partial \eta} + \frac{\partial^2 C_{\mathrm{B}}}{\partial \eta^2}\tilde{\eta}_s - \eta_{\mathrm{B},\xi}\frac{\partial \tilde{C}}{\partial \xi} - C_{\mathrm{B},\xi}(\xi,0)\tilde{\eta}_{s,\xi} \\ &\quad + \varepsilon W\hat{\mathrm{P}}\mathrm{e}(1-\kappa)C_{\mathrm{B}}(\xi,0)[\mathcal{G}^2(\xi,0)\tilde{\eta}_{s,t} - Y_\xi\tilde{\eta}_{s,\xi}] \\ &\quad + \varepsilon W\hat{\mathrm{P}}\mathrm{e}(1-\kappa)Y_\eta(\xi,0)\tilde{C} \\ &\quad + \varepsilon W\hat{\mathrm{P}}\mathrm{e}(1-\kappa)C_{\mathrm{B}}(\xi,0)Y_{\eta\eta}(\xi,0)\tilde{\eta}_s + (\text{h.o.t.}) = 0. \end{aligned} \tag{7}$$

IV. MULTIPLE-VARIABLE EXPANSION (MVE) SOLUTIONS OF PERTURBED STATES IN THE OUTER REGION

In order to find the asymptotic solutions for the perturbed states of the system derived in the last section, we apply the MVE method with the fast variables defined as

$$t_+ = \frac{\sigma t}{\beta(\varepsilon)}, \quad \xi_+ = \frac{\phi(\xi,\eta)}{\beta(\varepsilon)} = \frac{1}{\beta(\varepsilon)}\int_{\xi_0}^{\xi} k(\xi_1,\eta)d\xi_1,$$

$$\eta_+ = \frac{\psi(\xi,\eta)}{\beta(\varepsilon)} = \frac{1}{\beta(\varepsilon)}\int_0^{\eta} k(\xi,\eta_1)d\eta_1, \tag{8}$$

where the lower limit ξ_0 is to be specified later. It is seen that $\phi_\xi = \psi_\eta = k(\xi,\eta), \phi(\xi_0,\eta,\varepsilon) = 0, \psi(\xi,0,\varepsilon) = 0$. Furthermore, we assume that the pair of functions (ϕ,ψ) is subject to the Cauchy-Riemann condition, $\phi_\eta = -\psi_\xi = g(\xi,\eta), g(\xi,0) = g(\xi_0,\eta) = 0$, so that $g_\xi = k_\eta, g_\eta = -k_\xi$. It can be deduced that under the transformation of independent variables from (ξ,η) to (ξ_+,η_+), the form of Laplace equation will be invariant (see Refs. [38–41]).

The converted multiple-variable system is as follows:

$$(k^2+g^2)\left(\frac{\partial^2\tilde C}{\partial\xi_+^2}+\frac{\partial^2\tilde C}{\partial\eta_+^2}\right)+2\beta\left(k\frac{\partial^2}{\partial\xi_+\partial\xi}-g\frac{\partial^2}{\partial\eta_+\partial\xi}\right)\tilde C$$

$$+2\beta\left(g\frac{\partial^2}{\partial\xi_+\partial\eta}+k\frac{\partial^2}{\partial\eta_+\partial\eta}\right)\tilde C$$

$$=\varepsilon\beta W\hat{\mathrm{P}}\mathrm{e}\left[\mathcal{G}^2\sigma\frac{\partial}{\partial t_+}-Y_\xi\left(k\frac{\partial}{\partial\xi_+}-g\frac{\partial}{\partial\eta_+}+\beta\frac{\partial}{\partial\xi}\right)\right.$$

$$\left.-X_\xi\left(g\frac{\partial}{\partial\xi_+}+k\frac{\partial}{\partial\eta_+}+\beta\frac{\partial}{\partial\eta}\right)\right]\tilde C-\beta^2\left(\frac{\partial^2}{\partial\xi^2}+\frac{\partial^2}{\partial\eta^2}\right)\tilde C$$

$$(-1<\xi<0,-\infty<\xi_+<0;0\leqslant\eta,\eta_+<\infty), \tag{9}$$

with the following boundary conditions:

(1) Away from the interface, $\eta_+ \to +\infty$

$$\tilde C \to 0\,. \tag{10}$$

(2) At the side wall, $\xi = -1$ and $\xi_+ \to -\infty$

$$\frac{\partial\tilde C}{\partial\xi_+} = 0\,. \tag{11}$$

(3) On the interface, we may further make Taylor expansion for the solution $(\tilde C,\tilde\eta_{\mathrm s})$ around $\eta = \eta_+ = 0$. It follows that, at $\eta = \eta_+ = 0$,

$$\tilde C+\frac{\varepsilon h_1\bar k}{\beta}\frac{\partial\tilde C}{\partial\eta_+}$$

$$=-[C_{\mathrm B,\eta}(\xi,0)+\varepsilon W\hat{\mathrm P}\mathrm e\lambda_{\mathrm G}Y_\eta(\xi,0)]\tilde\eta_{\mathrm s}$$

$$+\frac{\varepsilon^2\bar k^2}{\beta^2(\varepsilon)\mathbb{M}W\mathcal{G}_0(\xi)}\frac{\partial^2\tilde\eta_{\mathrm s}}{\partial\xi_+^2}+(\text{h.o.t.}); \tag{12}$$

and

$$\left(\beta\frac{\partial\tilde C}{\partial\eta}+\bar k\frac{\partial\tilde C}{\partial\eta_+}\right)-\eta_{\mathrm B,\xi}\left(\beta\frac{\partial\tilde C}{\partial\xi}+\bar k\frac{\partial\tilde C}{\partial\xi_+}\right)+\beta\frac{\partial^2 C_{\mathrm B}}{\partial\eta^2}\tilde\eta_{\mathrm s}$$

$$-C_{\mathrm B,\xi}(\xi,0)\left(\beta\frac{\partial\tilde\eta_{\mathrm s}}{\partial\xi}+\bar k\frac{\partial\tilde\eta_{\mathrm s}}{\partial\xi_+}\right)+\varepsilon W\hat{\mathrm P}\mathrm e(1-\kappa)C_{\mathrm B}(\xi,0)$$

$$\times\left[\mathcal{G}_0^2(\xi)\left(\beta\frac{\partial\tilde\eta_{\mathrm s}}{\partial t}+\sigma\frac{\partial\tilde\eta_{\mathrm s}}{\partial t_+}\right)-Y_{\xi,0}(\xi)\left(\beta\frac{\partial\tilde\eta_{\mathrm s}}{\partial\xi}+\bar k\frac{\partial\tilde\eta_{\mathrm s}}{\partial\xi_+}\right)\right]$$

$$+\varepsilon\beta W\hat{\mathrm P}\mathrm e(1-\kappa)Y_\eta(\xi,0)\tilde C+\varepsilon\beta W\hat{\mathrm P}\mathrm e(1-\kappa)C_{\mathrm B}(\xi,0)Y_{\eta\eta}$$

$$\times(\xi,0)\tilde\eta_{\mathrm s}+(\text{h.o.t.})=0. \tag{13}$$

In the above, we have defined $\bar k = k(\xi,0)$ and the functions $\mathcal{G}_0(\xi)$ and $Y_{\xi,0}(\xi)$ are (see Refs. [35–37])

$$\mathcal{G}_0(\xi)=\mathcal{G}(\xi,0)=\sqrt{\lambda_0^2+(1-\lambda_0)^2\tan^2\left(\frac{\pi\xi}{2}\right)}$$

$$Y_{\xi,0}(\xi)=Y_\xi(\xi,0)=-(1-\lambda_0)\tan\left(\frac{\pi\xi}{2}\right). \tag{14}$$

(4) At the tip, $\xi = \xi_+ = 0$,

$$\tilde\eta_{\mathrm s}=0;\quad \beta\frac{\partial\tilde\eta_{\mathrm s}}{\partial\xi}+k\frac{\partial\tilde\eta_{\mathrm s}}{\partial\xi_+}=0. \tag{15}$$

(5) Root condition: Assume that away from the tip, as $\xi_+ \to \infty$, the perturbed state cannot be growing *exponentially*. Under this assumption it can be further shown that as $\xi_+ \to \infty$, the solution must be vanishing, namely,

$$\tilde h_0 \to 0. \tag{16}$$

In terms of the multiple variables $(\xi,\eta,\xi_+,\eta_+,t_+)$, we may write

$$C(\xi,\eta,t,\varepsilon)=C_{\mathrm B}(\xi,\eta,\varepsilon)+\tilde C(\xi,\eta,\xi_+,\eta_+,t_+,\varepsilon),$$

$$\eta_{\mathrm s}=\eta_{\mathrm B}(\xi,\varepsilon)+\tilde\eta_{\mathrm s}(\xi,\xi_+,t_+,\varepsilon), \tag{17}$$

and convert the system of Eq. (5) with the far-field condition, side-wall condition, and the interface conditions (6) and (7) into the form of a multiple-variable system. Furthermore, we may look for the following singular perturbed expansions (SPEs) for the following solutions:

$$\tilde C(\xi,\xi_+,\eta,\eta_+,t_+,\varepsilon)\sim\varepsilon[\tilde\mu_0(\varepsilon)\tilde C_0(\xi,\eta,\xi_+,\eta_+)$$

$$+\tilde\mu_1(\varepsilon)\tilde C_1(\xi,\eta,\xi_+,\eta_+)]\mathrm e^{t_+}+\cdots,$$

$$\tilde\eta_{\mathrm s}(\xi,\xi_+,\varepsilon)\sim[\tilde b_0(\varepsilon)\tilde h_0(\xi,\xi_+)+\tilde b_1(\varepsilon)\tilde h_1(\xi,\xi_+)+\cdots]\mathrm e^{t_+},$$

$$k(\xi,\eta,\varepsilon)\sim k_0(\xi,\eta)+\varepsilon k_1(\xi,\eta)+\cdots, \tag{18}$$

$$g(\xi,\eta,\varepsilon)\sim g_0(\xi,\eta)+\varepsilon g_1(\xi,\eta)+\cdots,$$

$$\bar k(\xi,\varepsilon)\sim\bar k_0(\xi)+\varepsilon\bar k_1(\xi)+\cdots,$$

$$\sigma(\varepsilon)\sim\sigma_0+\varepsilon\sigma_1+\cdots.$$

A. Leading-order SPE solution $O[\varepsilon\tilde{\mu}_0(\varepsilon)]$

In the leading-order approximation, we find $\tilde{b}_0(\varepsilon) = \tilde{\mu}_0(\varepsilon)$ and $\beta(\varepsilon) = \varepsilon^{\frac{1}{2}}$ and the equation

$$\frac{\partial^2 \tilde{C}_0}{\partial \xi_+^2} + \frac{\partial^2 \tilde{C}_0}{\partial \eta_+^2} = 0, \tag{19}$$

with the boundary conditions:

(1) In the far field away from the interface, $\eta_+ \to +\infty$, $\tilde{C}_0 \to 0$

(2) At the side wall, $\xi = 1$, $\frac{\partial \tilde{C}_0}{\partial \xi_+} = 0$

(3) At the interface $\eta = \eta_+ = 0$, we have

$$\tilde{C}_0 = -W\hat{\text{P}}\text{e}(\lambda_\text{G} - y_{*0} + 1)\tilde{h}_0 + \frac{\bar{k}_0^2}{\mathbb{M}W\mathcal{G}_0(\xi)}\frac{\partial^2 \tilde{h}_0}{\partial \xi_+^2} \tag{20}$$

and

$$\bar{k}_0 \frac{\partial \tilde{C}_0}{\partial \eta_+} + \sigma_0 W\hat{\text{P}}\text{e}(1-\kappa)y_{*0}\bar{\mathcal{G}}_0^2(\xi)\tilde{h}_0$$

$$+\bar{k}_0 W\hat{\text{P}}\text{e}[\lambda_\text{G} - (1-\kappa)y_{*0}]Y_{\xi,0}(\xi)\frac{\partial \tilde{h}_0}{\partial \xi_+} = 0, \tag{21}$$

where we have defined $\bar{k}_0 = k_0(\xi,0)$

(4) At the tip, $\xi = \xi_+ = 0$, $\frac{\partial \tilde{h}_0}{\partial \xi_+} = \tilde{h}_0 = 0$

(5) At the bottom of root, as $\xi_+ \to \infty$, $\tilde{h}_0 \to 0$.

We consider the normal mode solutions:

$$\tilde{C}_0 = \tilde{A}_0(\xi,\eta)\exp\left[\text{i}\xi_+ - \eta_+\right], \quad \tilde{h}_0 = \hat{D}_0 \exp\left[\text{i}\xi_+\right], \tag{22}$$

where the coefficient $\hat{D}_0$ is an arbitrary complex constant. The far-field condition is automatically satisfied, provided $\text{Re}\{k_0\} > 0$. Let $\hat{A}_0(\xi) = \tilde{A}_0(\xi,0)$. By substituting (22) into the interface conditions (20) and (21), we derive

$$\hat{A}_0(\xi) = -\left[W\hat{\text{P}}\text{e}(\lambda_\text{G} - y_{*0} + 1) + \frac{\bar{k}_0^2}{\mathbb{M}W\mathcal{G}_0(\xi)}\right]\hat{D}_0$$

and the dispersion formula:

$$\sigma_0 = \Sigma(\bar{k}_0,\xi) = \frac{\bar{k}_0}{\bar{\Lambda}_0\mathcal{G}_0^2(\xi)}\left\{[\lambda_0 + \text{i}Y_{\xi,0}(\xi)] - \frac{\bar{k}_0^2}{\bar{\Lambda}_1\mathcal{G}_0(\xi)}\right\}, \tag{23}$$

where $\bar{\Lambda}_0 = \frac{(1-\kappa)y_{*0}}{[(1-\kappa)y_{*0}-\lambda_\text{G}]} > 0$, $\bar{\Lambda}_1 = \mathbb{M}W^2\hat{\text{P}}\text{e}[(1-\kappa)y_{*0} - \lambda_\text{G}] > 0$. The dispersion formula (23) is a cubic polynomial of $\bar{k}_0$. It is the generalization of the well-known Mullins-Sekerka dispersion formula for the system of unidirectional solidification [2,3]. It is similar to the one we have derived for the system of dendritic growth [37,38,40,41]. For given complex parameter σ_0, one can solve for three complex wave numbers as functions of ξ: $\{\bar{k}_0^{(1)}(\xi),\bar{k}_0^{(2)}(\xi),\bar{k}_0^{(3)}(\xi)\}$.

B. Transformation of variables

For the further analysis of the dispersion formula (23), we employ the new variable ρ to replace ξ, which was first introduced for the investigation of the system of viscous fingering in 1997 (refer to Refs. [35–37]). Let

$$\rho = -\frac{Y_{\xi,0}(\xi)}{\lambda_0} = \left(\frac{1-\lambda_0}{\lambda_0}\right)\tan\left(\frac{\pi\xi}{2}\right). \tag{24}$$

It is seen that as $\xi \to 1^-$, $\rho \to \infty$. Thus, one may express $\mathcal{G}_0(\xi) = \lambda_0 S(\rho)$, where $S(\rho) = \sqrt{1+\rho^2}$. Moreover, one has

$$\text{d}\rho = -\frac{Y_{\xi\xi,0}}{\lambda_0}\text{d}\xi = \frac{\pi}{2}\frac{1-\lambda_0}{\lambda_0}\left[1 + \tan^2\left(\frac{\pi\xi}{2}\right)\right]d\xi,$$

$$\text{d}\xi = \frac{1}{G(\rho)}d\rho,$$

$$G(\rho) = -\frac{Y_{\xi\xi,0}(\xi)}{\lambda_0} = \frac{\pi}{2}\left(\frac{\lambda_0}{1-\lambda_0}\right)\left[\rho^2 + \left(\frac{1-\lambda_0}{\lambda_0}\right)^2\right]$$
$$= \frac{\pi}{2a}(\rho + \text{i}a)(\rho - \text{i}a), \tag{25}$$

where $a = \frac{1-\lambda_0}{\lambda_0}$. As demonstrated in Refs. [37], the new variable ρ is associated with the arclength $\ell(\xi)$ measured along the interface of the basic state starting from the tip $\xi = 0$. In fact, one can write $\ell(\xi) = \int_0^\xi \mathcal{G}_0(\xi_1)\text{d}\xi_1 = \int_0^\rho \mathcal{F}(\rho)\text{d}\rho$, where $\mathcal{F}(\rho) = \frac{\mathcal{G}_0(\xi)}{G(\rho)} = -\frac{\lambda_0\mathcal{G}_0(\xi)}{Y_{\xi\xi,0}(\xi)}$.

With the new variable ρ, one may express the perturbed solutions in the following form:

$$\tilde{h}_0(\xi) = \hat{D}_0 \exp\left[\frac{\text{i}}{\varepsilon^{\frac{1}{2}}}\int_{\xi_0}^{\xi}\bar{k}_0(\xi_1)\xi_1\right]$$
$$= \hat{D}_0 \exp\left[\frac{\text{i}}{\varepsilon^{\frac{1}{2}}}\int_{\rho_0}^{\rho}\tilde{k}_0(\rho_1)\rho_1\right] = \tilde{h}_0(\rho), \tag{26}$$

where $\bar{k}_0(\xi) = \tilde{k}_0(\rho)G(\rho)$, the lower limit $\rho_0 = \rho(\xi_0)$.

Furthermore, in terms of the wave number function $\tilde{k}_0(\rho)$ and variable ρ, the form of the dispersion formula becomes

$$\sigma_0 = \frac{G(\rho)\tilde{k}_0}{\bar{\Lambda}_0\lambda_0 S^2(\rho)}\left[(1-\text{i}\rho) - \frac{G^2(\rho)\tilde{k}_0^2}{\bar{\Lambda}_1\lambda_0^2 S(\rho)}\right]. \tag{27}$$

It can be further rewritten as

$$\sigma_\text{e} = \Sigma(k_\text{e},\rho) = \frac{k_\text{e}}{S^2(\rho)}\left[(1-\text{i}\rho) - \frac{k_\text{e}^2}{S(\rho)}\right], \tag{28}$$

provided that one sets $k_\text{e}(\rho) = \tilde{k}_0(\rho)\frac{G(\rho)}{\lambda_0\sqrt{\bar{\Lambda}_1}}$; $\sigma_\text{e} = \frac{\bar{\Lambda}_0}{\sqrt{\bar{\Lambda}_1}}\sigma_0$.

The form of (28) is exactly the same as the dispersion formulas that we have encountered in the system of dendritic growth with the one-sided model, as well as in the system of viscous fingering. This result indicates that the stability mechanisms of cellular growth have profound similarity with that of dendritic growth and viscous fingering.

For a given complex number σ_0, one may find three roots of (28), namely,

$$k_\text{e}^{(1)}(\rho) = M(\rho)\cos\left\{\frac{1}{3}\cos^{-1}\left[\frac{\sigma_\text{e}}{N(\rho)}\right]\right\} \quad \text{(SW branch)}$$

$$k_\text{e}^{(2)}(\rho) = M(\rho)\cos\left\{\frac{1}{3}\cos^{-1}\left[\frac{\sigma_\text{e}}{N(\rho)}\right] + \frac{2\pi}{3}\right\} \tag{29}$$

$$k_\text{e}^{(3)}(\rho) = M(\rho)\cos\left\{\frac{1}{3}\cos^{-1}\left[\frac{\sigma_\text{e}}{N(\rho)}\right] + \frac{4\pi}{3}\right\} \quad \text{(LW branch)},$$

where $M(\rho) = \sqrt{\frac{4S(\rho)}{3}}(1-\text{i}\rho)^{\frac{1}{2}}$ and $N(\rho) = -\frac{M(\rho)}{3S^2(\rho)}(1-\text{i}\rho)$. In the above, SW branch is referred to the short-wave

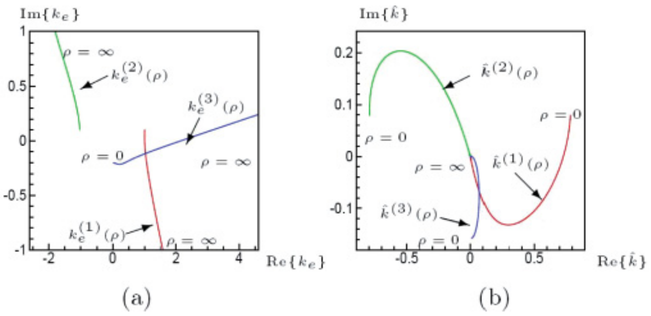

FIG. 5. (Color online) Typical dispersion curves for the case $\mathbb{M} = 0.4, \kappa = 0.2, \lambda_G = 3.748, \lambda_0 = 0.55$, and $\sigma_0 = (3.187 \times 10^{-4}, -5.882 \times 10^{-3}), \varrho_c = (1.0, -0.9847)$. (a) The variations of the wave-number function $k_e^{(i)}(\varrho)$. (b) The variations of the wave-number function $\hat{k}_0^{(i)}(\varrho) = \frac{k_e^{(i)}(\varrho)}{G(\varrho)} = \frac{\tilde{k}_0^{(i)}(\varrho)}{\lambda_0\sqrt{\bar{\Lambda}_1}}$.

branch,while LW branch is referred to the long-wave branch. The dispersion curves with $k_e^{(i)}(\rho)$ $(i = 1,2,3)$ are shown in Fig. 5(a) for a typical case. It is seen that as $\rho \to \infty$, we have $\mathrm{Im}\{k_e^{(1)}(\rho)\} < 0$ and $\mathrm{Im}\{k_e^{(3)}\}(\rho) > 0$, whereas the dispersion curves with $\hat{k}_0^{(i)}(\rho) = \frac{k_e^{(i)}(\varrho)}{G(\rho)} = \frac{\tilde{k}_0^{(i)}(\rho)}{\lambda_0\sqrt{\bar{\Lambda}_1}}$ $(i = 1,2,3)$ are shown in Fig. 5(b). When $\rho \gg 1$, all the points $\hat{k}_0^{(i)}(\rho),(i = 1,2,3)$ converge on the origin $\hat{k}_0 = 0$ from different directions.

The concentration field $\tilde{C}_0$ of the perturbed state given by the solution $H_2(\rho)$ having the wave function $k_e^{(2)}(\rho)$ cannot satisfy the far-field condition in the region away from the interface, due to $\mathrm{Re}\{\tilde{k}_0^{(2)}\} < 0$. As a consequence, the solution $H_2(\rho)$ must be ruled out. Only solutions $H_1(\rho)$ and $H_3(\rho)$ with $k_e^{(1)}(\rho)$, and $k_e^{(3)}(\rho)$ in (29), respectively, are meaningful. Here H_3, corresponding to the wave function $k_e^{(3)}(\rho)$ of the LW branch, is called as the long interfacial wave, whereas H_1, corresponding to the wave function $k_e^{(1)}(\rho)$ of the SW branch, is called the short interfacial wave. Thus, the general solution in the outer region is described as a combination of two fundamental interfacial traveling H waves:

$$\begin{aligned}\tilde{h}_0(\rho) &= D_1 H_1(\rho) + D_3 H_3(\rho)\\ &= D_1 \exp\left[\frac{\mathrm{i}}{\sqrt{\varepsilon}}\int_{\rho_0}^{\rho}\left(\tilde{k}_0^{(1)} + \varepsilon\tilde{k}_1^{(1)} + \cdots\right)d\rho_1\right]\\ &\quad + D_3 \exp\left[\frac{\mathrm{i}}{\sqrt{\varepsilon}}\int_{\rho_0}^{\rho}\left(\tilde{k}_0^{(3)} + \varepsilon\tilde{k}_1^{(3)} + \cdots\right)d\rho_1\right]. \end{aligned} \quad (30)$$

The constants D_1 and D_3 are to be determined. Note that $\mathrm{Im}\{\tilde{k}_0^{(1)}\} < 0$ and $\mathrm{Im}\{\tilde{k}_0^{(3)}\} > 0$, as $\rho \gg 1$. As a consequence, as $\rho \to \infty$ along the real axis, $H_1(\rho)$ is dominant, increasing exponentially, whereas $H_3(\rho)$ is subdominant, decreasing exponentially.

So far we have not yet applied the tip smoothness condition at $\rho = 0$ and the finiteness condition at the root, $\lim_{\rho\to\infty}|\tilde{h}_0(\rho)| < \infty$ for the perturbed states. It is seen that with a fixed pair of constant coefficients $\{D_1, D_3\}$, the solution (30) can never satisfy these two conditions simultaneously. To satisfy the root condition, the MVE solution can have only the subdominant component H_3, while to satisfy the tip condition, it must have both components H_1 and H_3. Hence we have the same dilemma as encountered in studying the systems of dendritic growth and viscous fingering formation. To resolve this dilemma, one must identify the singular points of the MVE solution and examine the behavior of the MVE solution near these singular points. It will be shown in the following sections that the MVE solution has a turning-point singularity in the extended complex ρ (or ξ) plane; associated with this singular point and due to the Stokes phenomenon, the pair of coefficients $\{D_1, D_3\}$ are piecewise constants along the real axis of ρ and on the complex ρ plane.

C. The first-order approximation and singularity of MVE solution

The first-order approximation solution will fully determine the amplitude $A_0(\xi,\eta)$, the functions $\bar{k}_1(\xi)$, and σ_1, whose detailed derivations are given in the Appendix. It is shown there that in order to derive the global uniformly valid asymptotic expansion solution, one must extend all the functions such as $\bar{k}_0(\xi)$, $Y_{\xi,0}(\xi)$, $\mathcal{G}_0(\xi)$, etc., by the analytical continuation, to the corresponding complex functions $\bar{k}_0(\zeta)$, $Y_{\zeta,0}(\zeta)$, $\mathcal{G}_0(\zeta)$, etc., in the complex plane $\zeta = \xi + \mathrm{i}\xi_I$, and the problem is to be analyzed in the extended space (ζ,η). As a consequence, the wave-number function $\bar{k}_0(\zeta) \equiv \{\bar{k}_0^{(1)}(\zeta), \bar{k}_0^{(2)}(\zeta), \bar{k}_0^{(3)}(\zeta)\}$ is subject to the extended dispersion formula:

$$\sigma_0 = \Sigma(\bar{k}_0,\zeta) = \frac{\bar{k}_0}{\bar{\Lambda}_0\mathcal{G}_0^2(\zeta)}\left\{[\lambda_0 + \mathrm{i}Y_{\zeta,0}(\zeta)] - \frac{\bar{k}_0^2}{\bar{\Lambda}_1\mathcal{G}_0(\zeta)}\right\}. \quad (31)$$

In accordance with the above, the function $\tilde{k}_0(\rho)$ is extended by the analytical continuation to the complex function $\tilde{k}_0(\varrho)$ in the complex plane $\varrho = \rho + \mathrm{i}\rho_I$ subject to the extended dispersion formula:

$$\sigma_e = \Sigma(k_e,\varrho) = \frac{k_e}{S^2(\varrho)}\left[(1 - \mathrm{i}\varrho) - \frac{k_e^2}{S(\varrho)}\right]. \quad (32)$$

It is then found that the MVE solution has a singular point $(\zeta_c,0)$ in the extended plane (ζ,η), or a singular point $(\varrho_c,0)$ in the extended plane (ϱ,η). The parameter ζ_c is subject to the following equation:

$$\frac{\partial\Sigma(\bar{k}_0,\zeta_c)}{\partial\bar{k}_0} = 0 \quad \text{and} \quad \left[\bar{k}_0^{(1)}(\zeta_c) - \bar{k}_0^{(3)}(\zeta_c)\right] = 0, \quad (33)$$

whereas the parameter ϱ_c is subject to the following equation:

$$\frac{2}{\sqrt{27}}\left(\frac{1 - \mathrm{i}\varrho_c}{1 + \mathrm{i}\varrho_c}\right)^{3/4} = \frac{\bar{\Lambda}_0}{\sqrt{\bar{\Lambda}_1}}\sigma_0. \quad (34)$$

It is obtained that

$$\begin{aligned}\sigma_1 = \frac{1}{W\hat{\mathrm{P}}\mathrm{e}(1-\kappa)y_{*0}\mathcal{G}_0^2(\zeta_c)}\Bigg\{&W\hat{\mathrm{P}}\mathrm{e}[\lambda_G - (1-\kappa)y_{*0}]\\ &\times Y_{\eta\eta}(\zeta_c,0) - \frac{\mathrm{i}F_0(\zeta_c)\mathcal{G}_0'(\zeta_c)}{3\mathcal{G}_0(\zeta_c)}\Bigg\},\end{aligned} \quad (35)$$

where

$$\begin{aligned}F_0(\zeta) = &-W\hat{\mathrm{P}}\mathrm{e}(\lambda_G - y_{*0} + 1) + \mathrm{i}W\hat{\mathrm{P}}\mathrm{e}\\ &\times[(1-\kappa)y_{*0} - \lambda_G]Y_{\xi,0}(\zeta).\end{aligned} \quad (36)$$

The formula (35) shows that once σ_0 is known, σ_1 follows. However, up to this point, the parameter σ_0 still remains free. In the next section, we shall study the behavior of a solution near the singular point ζ_c and derive the parameter σ_0 and the global wave modes solutions in the extended (ζ,η) space.

V. THE INNER SOLUTION IN THE VICINITY OF SINGULAR POINT (ζ_c,0)

The fact that the MVE solution is not valid at the point $(\zeta_c,0)$ in the extended (ζ,η) space implies that the solutions in the vicinity of the point $(\zeta_c,0)$ in the (ζ,η) space, $|\zeta-\zeta_c|\ll 1$, $|\eta|\ll 1$, no longer have the multiple length scales. Thus, to derive the inner solution near the point $(\zeta_c,0)$, one must start with the associated homogenous system (5)–(7), and seek a different asymptotic form of the solution. In doing so, we introduce the inner variables

$$\zeta_*=\frac{\zeta-\zeta_c}{\varepsilon^\alpha},\quad \eta_*=\frac{\eta}{\varepsilon^\alpha}, \tag{37}$$

where the exponent α is to be determined later. With the inner variables, the interface shape function is expressed as $\tilde{\eta}_s(\zeta,t,\varepsilon)=\varepsilon^\alpha\tilde{\eta}_{*s}(\zeta_*,t_+,\varepsilon)$, while the concentration of impurity is expressed as $\tilde{C}(\zeta,\eta,t,\varepsilon)=\varepsilon^\alpha\tilde{C}_*(\zeta_*,\eta_*,t_+,\varepsilon)$.

The inner system is derived as

$$\left(\frac{\partial^2}{\partial\zeta_*^2}+\frac{\partial^2}{\partial\eta_*^2}\right)\tilde{C}_*+\varepsilon^{\alpha+1}W\hat{\text{P}}\text{e}\left[Y_\xi\frac{\partial\tilde{C}_*}{\partial\zeta_*}+X_\xi\frac{\partial\tilde{C}_*}{\partial\eta_*}\right.$$
$$\left.+\mathcal{G}^2\frac{\sigma}{\beta(\varepsilon)}\frac{\partial\tilde{C}_*}{\partial t_+}\right]=0, \tag{38}$$

with the following interface conditions: at $\eta_*=0$,

$$\tilde{C}_*=-\varepsilon W\hat{\text{P}}\text{e}\,[\lambda_{\text{G}}-(y_{*0}-1)]\,\tilde{\eta}_{*s}$$
$$+\frac{\varepsilon^{2(1-\alpha)}}{\mathbb{M}W\mathcal{G}_0(\zeta)}\frac{\partial^2\tilde{\eta}_{*s}}{\partial\zeta_*^2}+\text{(h.o.t.)}, \tag{39}$$

and

$$\frac{\partial\tilde{C}_*}{\partial\eta_*}+\varepsilon W\hat{\text{P}}\text{e}Y_{\xi,0}(\zeta)\,[\lambda_{\text{G}}-(1-\kappa)y_{*0}]\,\frac{\partial\tilde{\eta}_{*s}}{\partial\zeta_*}$$
$$+\varepsilon^{1+\alpha}W\hat{\text{P}}\text{e}(1-\kappa)y_{*0}\mathcal{G}_0^2(\zeta)\frac{\sigma}{\beta(\varepsilon)}\frac{\partial\tilde{\eta}_{*s}}{\partial t_+}$$
$$+\text{(h.o.t.)}=0. \tag{40}$$

We make the following inner expansions for the solution:

$$\tilde{C}_*(\zeta_*,\eta_*,t_+,\varepsilon)=\varepsilon[\tilde{\nu}_0(\varepsilon)\tilde{Y}_{*0}(\zeta_*,\eta_*)$$
$$+\tilde{\nu}_1(\varepsilon)\tilde{Y}_{*1}(\zeta_*,\eta_*)+\cdots]\text{e}^{t_+}$$
$$\tilde{\eta}_{*s}(\zeta_*,t_+,\varepsilon)=[\tilde{\nu}_0(\varepsilon)\tilde{h}_{*0}(\zeta_*)+\tilde{\nu}_1(\varepsilon)\tilde{h}_{*1}(\zeta_*)$$
$$+\cdots]\text{e}^{t_+}. \tag{41}$$

A. Leading-order inner solution in the vicinity of ζ_c

By dropping higher-order small terms contained in the system (39) and (40), it follows that

$$\frac{\partial^2\tilde{C}_{*0}}{\partial\zeta_*^2}+\frac{\partial^2\tilde{C}_{*0}}{\partial\eta_*^2}=0, \tag{42}$$

with the boundary conditions: At the interface $\eta_*=0$, we have

$$\tilde{C}_{*0}=-W\hat{\text{P}}\text{e}[\lambda_{\text{G}}-(y_{*0}-1)]\tilde{h}_{*0}+\frac{\varepsilon^{1-2\alpha}}{\mathbb{M}W\mathcal{G}_0(\zeta)}\frac{\partial^2\tilde{h}_{*0}}{\partial\zeta_*^2} \tag{43}$$

and

$$\frac{\partial\tilde{C}_{*0}}{\partial\eta_*}+W\hat{\text{P}}\text{e}[\lambda_{\text{G}}-(1-\kappa)y_{*0}]Y_{\xi,0}(\zeta)\frac{\partial\tilde{h}_{*0}}{\partial\zeta_*}$$
$$+\varepsilon^{\alpha-\frac{1}{2}}\sigma_0W\hat{\text{P}}\text{e}(1-\kappa)y_{*0}\mathcal{G}_0^2(\zeta)\tilde{h}_{*0}=0. \tag{44}$$

More higher-order small terms shall be dropped later. Due to the analyticity of the solution, one has $\frac{\partial\tilde{C}_{*0}}{\partial\eta_*}=\text{i}\frac{\partial\tilde{C}_{*0}}{\partial\zeta_*}$. Applying this formula at the interface $\eta=0^+$, from (43) and (44) we derive

$$\varepsilon^{1-2\alpha}\frac{\text{d}^3\tilde{h}_{*0}}{\text{d}\zeta_*^3}+\bar{\Lambda}_1\mathcal{G}_0(\zeta)[\lambda_0+\text{i}Y_{\xi,0}(\zeta)]\frac{\text{d}\tilde{h}_{*0}}{\text{d}\zeta_*}$$
$$-\text{i}\varepsilon^{\alpha-\frac{1}{2}}\sigma_0\mathbb{M}W^2\hat{\text{P}}\text{e}(1-\kappa)y_{*0}\mathcal{G}_0^3(\zeta)\tilde{h}_{*0}+\text{(h.o.t.)}=0. \tag{45}$$

With the variable ϱ and the corresponding inner variable $\varrho_*=\frac{\varrho-\varrho_c}{\varepsilon^\alpha}$, one may rewrite (45) in the following form:

$$\varepsilon^{1-2\alpha}G^3(\varrho)\frac{\text{d}^3\tilde{h}_{*0}}{\text{d}\varrho_*^3}+\lambda_0^2\bar{\Lambda}_1G(\varrho)S(\varrho)(1-\text{i}\varrho)\frac{\text{d}\tilde{h}_{*0}}{\text{d}\varrho_*}$$
$$-\text{i}\varepsilon^{\alpha-\frac{1}{2}}\sigma_0\mathbb{M}W^2\hat{\text{P}}\text{e}(1-\kappa)y_{*0}\lambda_0^3S^3(\varrho)\tilde{h}_{*0}$$
$$+\text{(h.o.t.)}=0. \tag{46}$$

In order to solve the above third-order ODE, we follow the approach developed in Refs. [37–39]. We first apply the following transformation for the solution in the outer region and the solution in the inner region, respectively; namely,

$$\tilde{h}_0(\varrho)=\tilde{W}_0(\varrho)\ \exp\left[\frac{\text{i}}{\sqrt{\varepsilon}}\int_{\varrho_c}^{\varrho}\tilde{k}_c(\varrho_1)d\varrho_1\right],$$
$$\tilde{h}_{*0}(\varrho_*)=\tilde{W}_{*0}(\varrho_*)\exp\left[\frac{\text{i}}{\sqrt{\varepsilon}}\int_{\varrho_c}^{\varrho}\tilde{k}_c(\varrho_1)d\varrho_1\right]. \tag{47}$$

The reference wave-number function $\tilde{k}_c(\varrho)$ is to be given later, and it satisfies the inequalities $\text{Re}\{\tilde{k}_0^{(3)}\}<\text{Re}\{\tilde{k}_c\}<\text{Re}\{\tilde{k}_0^{(1)}\}$. With the above transformation, in the outer region the solution $\tilde{h}_0$ can be considered as a combination of two W waves instead of two H waves; namely, we can write

$$\tilde{W}_0(\varrho)=D_1\tilde{W}_0^{(+)}(\varrho)+D_3\tilde{W}_0^{(-)}(\varrho), \tag{48}$$

where

$$\tilde{W}_0^{(+)}(\varrho)=H_1(\varrho)\exp\left\{-\frac{\text{i}}{\varepsilon^{\frac{1}{2}}}\int_{\varrho_c}^{\varrho}\tilde{k}_c(\varrho_1)d\varrho_1\right\}$$
$$\tilde{W}_0^{(-)}(\varrho)=H_3(\varrho)\exp\left\{-\frac{\text{i}}{\varepsilon^{\frac{1}{2}}}\int_{\varrho_c}^{\varrho}\tilde{k}_c(\varrho_1)d\varrho_1\right\}. \tag{49}$$

Here $\tilde{W}^{(+)}$ corresponding to the short H wave $H_1(\varrho)$ is now an outgoing W wave, while $\tilde{W}^{(-)}$ corresponding to the long H wave $H_3(\varrho)$ is now an incoming W wave.

We choose the reference wave-number function $\tilde{k}_c$ from the condition $(\frac{\partial\Sigma}{\partial\tilde{k}_0})_{\tilde{k}_0=\tilde{k}_c}=0$, such that

$$\tilde{k}_c(\varrho)=\frac{\sqrt{\frac{\lambda_0^2\bar{\Lambda}_1S}{3}(\,1-\text{i}\varrho)}}{G(\varrho)}$$
$$=\frac{\text{e}^{-\frac{i\pi}{4}}\bar{\Lambda}_1^{\frac{1}{2}}\lambda_0(\varrho-\text{i})^{\frac{1}{4}}(\varrho+\text{i})^{\frac{1}{4}}(\varrho+\text{i})^{\frac{1}{2}}}{3^{\frac{1}{2}}G(\varrho)}. \tag{50}$$

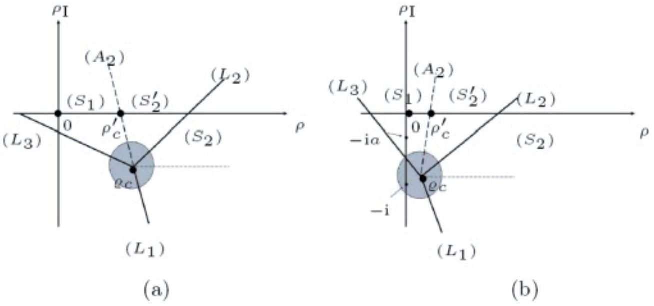

FIG. 6. Sketch of the Stokes and anti-Stokes lines emanating from ζ_c: (a) for the case I, $\sigma_0 = O(1)$; (b) for the case II, $|\sigma_0| \ll 1$.

From (46), one may derive the governing equation for the function $\tilde{W}_{*0}(\varrho_*)$ as follows:

$$\begin{aligned}&\varepsilon^{1-2\alpha} G^3(\varrho)\frac{\mathrm{d}^3\tilde{W}_{*0}(\varrho_*)}{\mathrm{d}\varrho_*^3} + \mathrm{i}\varepsilon^{\frac{1}{2}-\alpha}\lambda_0 G^2(\varrho)\\ &\times\sqrt{3\bar{\Lambda}_1 S(\varrho)(1-\mathrm{i}\varrho)}\frac{\mathrm{d}^2\tilde{W}_{*0}(\varrho_*)}{\mathrm{d}\varrho_*^2}\\ &-\mathrm{i}\varepsilon^{\alpha-\frac{1}{2}}\mathbb{M}W^2\hat{\mathrm{P}}\mathrm{e}(1-\kappa)y_{*0}\lambda_0^3 S^3(\varrho)\\ &\times[\sigma_0 - \Omega_0(\varrho)]\tilde{W}_{*0}(\varrho_*) + (\mathrm{h.o.t.}) = 0,\end{aligned} \tag{51}$$

where

$$\Omega_0(\varrho) = \frac{2}{\sqrt{27}}\frac{\sqrt{\bar{\Lambda}_1}}{\bar{\Lambda}_0}\frac{(1-\mathrm{i}\varrho)^{\frac{3}{2}}}{S^{\frac{3}{2}}(\varrho)} = \Sigma(\tilde{k}_c,\varrho). \tag{52}$$

It is now clearly seen that the equation (51) has five isolated singular points and turning points: $\varrho = \pm\mathrm{i}, \pm\mathrm{i}a$ and $\varrho = \varrho_c$, where ϱ_c is a simple turning point of (51) in the complex ϱ plane, and $\varrho = \pm\mathrm{i}, \pm\mathrm{i}a$ are roots of the functions of $S(\varrho)$ and $G(\varrho)$, respectively. In view of

$$\sigma_0 = \Omega_0(\varrho_c) = \frac{2}{\sqrt{27}}\frac{\sqrt{\bar{\Lambda}_1}}{\bar{\Lambda}_0}\left(\frac{1-\mathrm{i}\varrho_c}{1+\mathrm{i}\varrho_c}\right)^{3/4}, \tag{53}$$

to study the behavior of the inner solution in the vicinity of the turning point ϱ_c, one needs to distinct two different cases: case I: $|\sigma_0| = O(1)$; case II: $|\sigma_0| \ll 1$. The location of turning point ϱ_c and the corresponding Stokes lines and anti-Stokes lines emitted from ϱ_c are sketched in Fig. 6 for each case. In particular, it is seen that the cell's tip $\xi = 0$ and the bottom of root $\xi = 1$ are, respectively, located in different sectors: (S_1) and (S_2'), separated by the anti-Stokes line (A_2).

It is derived that in the far field of the vicinity of ϱ_c, the inner equation can be reduced to the general Airy equation:

$$\frac{\mathrm{d}^2\tilde{W}_{*0}(\hat{\varrho}_*)}{\mathrm{d}\hat{\varrho}_*^2} + \hat{\varrho}_*^{p_0}\tilde{W}_{*0}(\hat{\varrho}_*) = 0, \tag{54}$$

and the leading-order approximation of inner solution has the form $\tilde{W}_{*0}(\hat{\varrho}_*) = D_*\hat{\varrho}_*^{\frac{1}{2}}H_\nu^{(2)}(z)\,(z = 2\nu\hat{\varrho}_*^{\frac{1}{2\nu}};\ \nu = \frac{1}{p_0+2})$. Here the new variable $\hat{\varrho}_* = \mathbb{A}\varrho_*$ is used with the constant $\mathbb{A} = O(1)$. Moreover, it is derived that

(1) For case I $[|\sigma_0| = O(1)]$: We have $p_0 = 1, \theta_L = \frac{2}{3}\pi, \alpha = \frac{1}{3}, \nu = \frac{1}{3}$.

(2) For case II ($|\sigma_0| \ll 1$): We have $p_0 = \frac{7}{4}, \theta_L = \frac{8}{15}\pi, \alpha = \frac{2}{7}, \nu = \frac{4}{15}$.

In the above θ_L is the open angle between two Stokes lines and anti-Stokes lines. By matching the inner solution with the outer solution in the sector (S_1), the connection conditions for both cases are finally obtained in the unified form:

(1) In the domain: $\varrho \in (S_1)$; $\rho \in (0,\rho_c')$, we have

$$\frac{D_1}{D_3} = 2\mathrm{e}^{\mathrm{i}\frac{\pi}{2}}\cos(\nu\pi), \quad D_3 = D_3' \tag{55}$$

(2) In the domain: $\varrho \in (S_2)' \cup (S_2)$; $\rho \in (\rho_c',\infty)$, we have

$$D_1 = 0, \quad D_3 = D_3', \tag{56}$$

where ρ_c' is the intersection point of the anti-Stokes line (A_2) with the real axis of ϱ.

Up to now, we have not applied the tip smoothness condition. When the tip smoothness conditions are applied, the eigenvalue σ_0 will be determined as a function of the stability parameter ε and other physical parameters.

VI. GLOBAL INSTABILITY MECHANISMS

A. Spectrum of complex eigenvalues and global trapped wave (GTW) instability

Let us consider case I first. Case I leads to a spectrum of complex eigenvalues $\sigma_0 = \sigma_{0,\mathrm{R}} - \mathrm{i}\omega_0$ with $\omega_0 > 0$. The physical solution in the interval (S_1) of the outer region is $\mathrm{Re}\{\tilde{h}_0(\varrho,t)\} = \mathrm{Re}\{H(\varrho)\mathrm{e}^{\frac{\sigma_0 t}{\sqrt{\varepsilon}}}\}$, where $H(\varrho) = D_1H_1 + D_3H_3$. Let $d_1 = D_1\mathrm{e}^{-\mathrm{i}\chi_1}$, $d_3 = D_3\mathrm{e}^{-\mathrm{i}\chi_3}$, where $\chi_1 = \frac{1}{\sqrt{\varepsilon}}\int_0^{\varrho_c}\tilde{k}_0^{(1)}d\varrho$, $\chi_3 = \frac{1}{\sqrt{\varepsilon}}\int_0^{\varrho_c}\tilde{k}_0^{(3)}d\varrho$. Thus, it follows from the connection condition (55) that

$$\frac{d_1}{d_3} = \mathrm{i}\mathrm{e}^{-\mathrm{i}\chi}, \tag{57}$$

where $\chi = \frac{1}{\sqrt{\varepsilon}}\int_0^{\varrho_c}(\tilde{k}_0^{(1)} - \tilde{k}_0^{(3)})\mathrm{d}\varrho$. To satisfy the tip's smoothness conditions, the constants d_1 and d_3 must be subject to the following conditions:

$$\begin{aligned}\frac{d_3}{d_1} &= -\frac{\tilde{k}_0^{(1)}(0)}{\tilde{k}_0^{(3)}(0)} \quad &&\text{(for symmetrical S modes)}\\ d_1 &= \quad -d_3 &&\text{(for antisymmetrical A modes).}\end{aligned} \tag{58}$$

Combining (57) with (58), respectively, one obtains the following quantization condition:

$$\begin{aligned}\frac{1}{\sqrt{\varepsilon}}\int_0^{\varrho_c}(\tilde{k}_0^{(1)} - \tilde{k}_0^{(3)})d\varrho &= \left(2n + 1 + \frac{1}{2} + \theta_0\right)\pi\\ &\quad -\mathrm{i}\ln\alpha_0 \quad (n = 0,1,2,\ldots),\end{aligned} \tag{59}$$

where

$$\begin{aligned}\alpha_0\,\mathrm{e}^{\mathrm{i}\theta_0\pi} &= \frac{\tilde{k}_0^{(1)}(0)}{\tilde{k}_0^{(3)}(0)} \quad &&\text{(for S modes)}\\ \alpha_0 = 1,\ \theta_0 &= 0 &&\text{(for A modes).}\end{aligned} \tag{60}$$

The quantization condition (59) determines the spectrum of complex eigenvalues with $|\sigma_0| = O(1)$: $\{\sigma_{0,n}\}$ $(n = 0,1,2,\ldots)$, as functions of the parameters of λ_0 and ε. Such a spectrum of complex eigenvalues yields two discrete sets of eigenmodes: S modes and A modes. Given $\lambda_0, \hat{\mathrm{P}}\mathrm{e}$, and other physical parameters, the system allows a set of neutrally stable modes ($\sigma_{\mathrm{R}} = 0$) when $\varepsilon = \varepsilon_{*,n}$ $(n = 0,1,2,\ldots)$ with

$\varepsilon_* = \varepsilon_{*,0} > \varepsilon_{*,1} > \varepsilon_{*,2} > \cdots$. As ε in the range $\varepsilon_{*,k} < \varepsilon_* < \varepsilon_{*,k-1}$ where $k = 1,2,\ldots$, the system allows k unstable GTW modes with the indexes $k = 0,1,\ldots,k-1$, respectively. When $\varepsilon = \varepsilon_{*,k}$, the system allows a neutral stable mode with the index $n = k$, whose interface is oscillatory with the constant eigenfrequency $\omega_{*,k}$.

These eigenmodes are very similar to these *global traveling wave* (GTW) modes previously derived for dendritic growth, describing traveling waves propagating along the interface (see Refs. [37–39]). Therefore, we may also call this global oscillatory instability mechanism the global traveling wave mechanism.

It should be noted that under the current notation, the parameters $\varepsilon,\lambda_{\mathrm{G}}$ depend on both operation conditions: the pulling velocity V and the temperature gradient $(G)_{\mathrm{D}}$. In order to examine the effect of each of the operation conditions on the eigenvalue σ_0 separately, it is better to utilize the new control parameters: $\varepsilon_{\mathrm{c}} = \sqrt{\ell_{\mathrm{c}} V/\kappa_{\mathrm{D}}}$, which measures the pulling velocity V, and $G_{\mathrm{c}} = \frac{\ell_{\mathrm{c}}}{\ell_{\mathrm{G}}}$, which measures the gradient of temperature. Thus, one may write $\lambda_{\mathrm{G}} = G_{\mathrm{c}}/\varepsilon_{\mathrm{c}}^2$; $\hat{\mathrm{P}}\mathrm{e} = \varepsilon_{\mathrm{c}}^2/\varepsilon^3$; $\bar{\Lambda}_1 = \mathbb{M}W^2[(1-\kappa)y_{*0} - \frac{G_{\mathrm{c}}}{\varepsilon_{\mathrm{c}}^2}]\frac{\varepsilon_{\mathrm{c}}^2}{\varepsilon^3}$. The system is now controlled by three independent operation parameters: $\{\varepsilon_{\mathrm{c}},G_{\mathrm{c}},\mathbb{M}\}$ separately.

In Fig. 7(a) and 7(b), we show the variations of $\sigma_{0,\mathrm{R}} = \mathrm{Re}\{\sigma_0\}$ and $\omega_0 = |\mathrm{Im}\{\sigma_0\}|$ of the S-modes with ε for $n = 0,1,2$ under a typical operation condition in the zeroth-order approximation. It is seen that given ε, the growth rate of the S-mode with index n_i is greater than the S-mode with index n_j, if $n_i < n_j$. In this sense we call the S-mode $(n = n_i)$ more dangerous than the S-mode $(n = n_j)$. We have also calculated the quantization condition for A-modes and found that, with the same index n, the S-mode is more dangerous than the A-mode. Therefore, it is concluded that in the GTW mechanism the most dangerous mode is the S-mode with $n = 0$. By using the condition $\mathrm{Re}\{\sigma_0\} = 0$, one may determine the zeroth-order approximate value of the critical surface tension parameter $\varepsilon_* = \varepsilon_*^{(0)}$ and the associated eigenfrequency $\omega_*^{(0)}$. In the first-order approximation, one may set the eigenvalue $\sigma \approx \sigma_0 + \varepsilon\sigma_1$, and calculate the first-order approximate critical stability parameter $\varepsilon_* = \varepsilon_*^{(1)}$ and the associated eigenfrequency $\omega_*^{(1)}$ via the condition $\mathrm{Re}\{\sigma_0 + \varepsilon\sigma_1\} = 0$.

In Fig. 8(a) we compare the zeroth- and first-order approximations of the neutral curves of GTW-S-modes $(n = 0)$ in the (ε,λ_0) plane for a typical case, and in Fig. 9(a) we compare the zeroth- and first-order approximations of the associated eigenfrequency $\omega_*^{(0)}$ and $\omega_*^{(1)}$ versus λ_0. It is seen that with a fixed λ_0 we have $\varepsilon_*^{(1)} < \varepsilon_*^{(0)}$ and $\omega_*^{(1)} > \omega_*^{(0)}$.

In Fig. 10 we show the corresponding interface shape of a basic state added with the GTW-S-neutral mode $(n = 0)$. Since the interface shape of the GTW-S neutral mode has a self-sustaining side-branching structure, and the associated basic state has a needlelike tip with the relative width normally in the range $(0 < \lambda_0 < 0.5)$, one may call the GTW neutral curve the needlelike branch.

Note that the parameter ε is determined by the tip radius ℓ_{t}, while the relative width parameter λ_0 depends on both the tip radius ℓ_{t} and the primary spacing ℓ_w. To compare the experimental data, it is better to express the neutral curves in the dimensionless control parameters $(\hat{\ell}_{\mathrm{t}},\hat{\ell}_w)$ plane, where we define $\hat{\ell}_{\mathrm{t}} = \ell_{\mathrm{t}}/\ell_{\mathrm{c}}$ and $\hat{\ell}_w = \ell_w/\ell_{\mathrm{c}}$. The neutral curves given in Fig. 8(a) are shown in Fig. 8(b). The curves of ω_* shown in Fig. 9(a) are shown in Fig. 9(b).

The variation of the neutral curve of GTW-S $(n = 0)$ in the first-order approximation with the temperature gradient G_{D} and puling velocity V, $\mathbb{M}$, and κ are shown on the (ε,λ_0) plane in Fig. 11(a) and 11(b) and Fig. 12(a) and 12(b), respectively. For the same cases, these neutral curves are also shown on the $(\hat{\ell}_w,\hat{\ell}_{\mathrm{t}})$ plane in Fig. 13(a) and 13(b) and Fig. 14(a) and 14(b), respectively. It is seen that the smaller the temperature gradient G_{D}, the bigger pulling velocity V, the smaller the parameter κ, and the bigger the parameter $\mathbb{M}$, the more unstable the system. Furthermore, the variations of the eigenfrequency $\omega_*^{(1)}$ with G_{D}, V, and κ are shown in Fig. 15(a) and 15(b), respectively. It is seen that the smaller the temperature gradient G_{D}, the bigger pulling velocity V and the bigger eigenfrequency $\omega_*^{(1)}$.

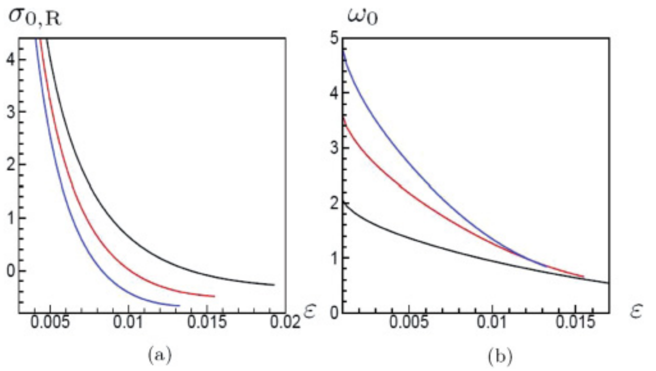

(a) (b)

FIG. 7. (Color online) The eigenvalues of GTW modes calculated in terms of the quantization condition (59) for the case $\varepsilon_{\mathrm{c}} = 0.01, \mathbb{M} = 0.08, \kappa = 0.3, G_{\mathrm{c}} = 2.0 \times 10^{-5}, \lambda_{\mathrm{G}} = 0.2, \lambda_0 = 0.45$, and $W_0 = 2.1332$. (a) The variations of the rear part of eigenvalue $\sigma_{0,\mathrm{R}} = \mathrm{Re}\{\sigma_0\}$ of GTW-S-modes $(n = 0,1,2)$ with ε from top to bottom. (b) The variation of the imaginary part of eigenvalue $\omega_0 = |\mathrm{Im}\{\sigma_0\}|$ of GTW-S-modes $(n = 0,1,2)$ with ε from bottom to top.

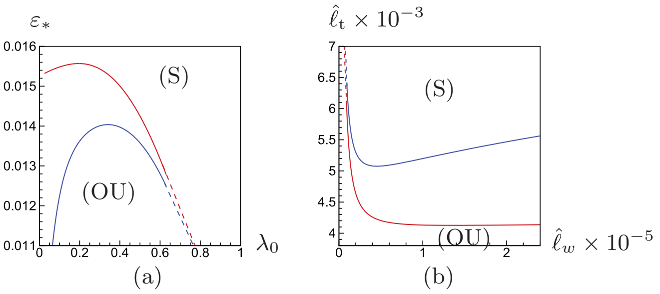

(a) (b)

FIG. 8. (Color online) Under the operation condition, $\varepsilon_{\mathrm{c}} = 0.5388 \times 10^{-2}$, $\mathbb{M} = 0.09552$, $\kappa = 0.29$, $G_{\mathrm{c}} = 0.11485 \times 10^{-4}$, $\lambda_{\mathrm{G}} = 0.4989$, which corresponds to $V = 16\ \mu\mathrm{m/s}, G_{\mathrm{D}} = 140^{-4}$ K/μm, in the zeroth- and first-order approximations from top to bottom. (a) The neutral curves of the GTW-(S)-modes $(n = 0)$ on the (λ_0,ε) plane; (b) the neutral curves of the GTW-(S)-modes $(n = 0)$ on the $(\hat{\ell}_w,\hat{\ell}_{\mathrm{t}})$ plane.

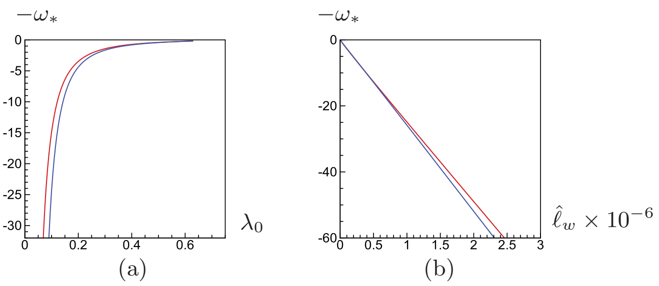

FIG. 9. (Color online) For the case, $\varepsilon_c = 0.5388 \times 10^{-2}$, $\mathbb{M} = 0.09552$, $\kappa = 0.29$, $G_c = 0.11485 \times 10^{-4}$, $\lambda_G = 0.4989$, in the zeroth- and first-order approximations from top to bottom. (a) The variations of $\mathrm{Im}\{\sigma_0\} = -\omega_0$ for the GTW-(S) neutral modes ($n = 0$) with λ_0. (b) The variations of $\mathrm{Im}\{\sigma_0\} = -\omega_0$ for the GTW-(S) neutral modes ($n = 0$) with $\hat{\ell}_w$.

B. Oscillatory stability criterion

From the above analysis, with given growth condition described by the three parameters ε_c, G_c, and $\mathbb{M}$, which, respectively, measure the puling velocity V, gradient of temperature G_D, and concentration of impurity in far field C_∞, the neutral curve of the GTW-S- ($n = 0$) mode divides the parameters (ε,λ_0), or $(\hat{\ell}_t,\hat{\ell}_w)$ plane into two regions: the (S) region and (OU) region. Accordingly, the basic state of the system is subject the oscillatory stability criterion:

$$\begin{aligned} &(\varepsilon,\lambda_0);\ (\hat{\ell}_t,\hat{\ell}_w) \in (\mathrm{S})\text{: stable} \\ &(\varepsilon,\lambda_0);\ (\hat{\ell}_t,\hat{\ell}_w) \in (\mathrm{OU})\text{: oscillating unstable.} \end{aligned} \quad (61)$$

C. Spectrum of real eigenvalues and low-frequency (LF) instability

Case II leads to a spectrum of real eigenvalues with $|\sigma_0| \ll 1$. For this case the physical solution in the outer region is given as $\mathrm{Re}\{\tilde{h}(\varrho,t)\} = \mathrm{Re}\{H(\varrho)\}e^{\frac{\sigma_0 t}{\sqrt{\varepsilon}}}$. The system allows two types of global LF modes.

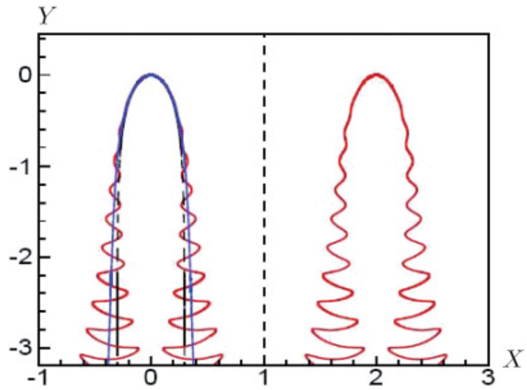

FIG. 10. (Color online) The arrayed-dendritic interface shape of the neutral GTW-(S)-modes ($n = 0$) calculated by using the formulas (26), (48), and (55) for the case $\varepsilon_c = 0.119 \times 10^{-2}, \kappa = 0.1, G_c = 6.9 \times 10^{-7}$, $\lambda_G = 4.872 \times 10^{-3}$, $\mathbb{M} = 0.50$, and $\lambda_0 = 0.3$. The dashed line closer to the centerline of dendrite is the Saffman-Taylor solution; the solid line outside of the Saffman-Taylor solution is the first-order approximation of the basic state solution.

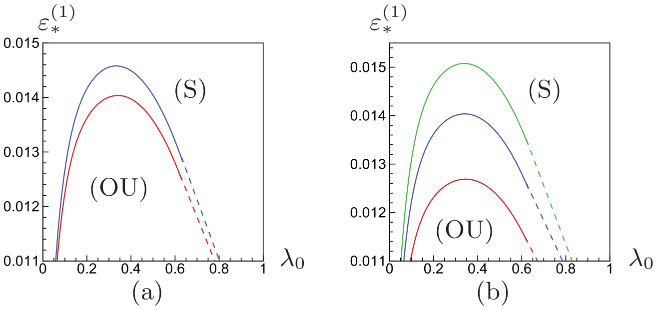

FIG. 11. (Color online) (a) The neutral curves of the GTW-(S)-modes ($n = 0$) in first-order approximation on the (ε,λ_0) plane calculated by using the formulas (35) and (59) for the cases of the concentration of impurity $C_\infty = 1.2$ mole%, the pulling velocity $V = 16$ μm/s and various values of temperature gradient $G_D = 78 \times 10^{-4}$Kμm, 140×10^{-4}K/μm, which corresponds to the cases: $\varepsilon_c = 0.5388 \times 10^{-2}$, $\mathbb{M} = 0.9552$, $\kappa = 0.29$, and $G_c = 0.8070 \times 10^{-5}$, 0.1448×10^{-4}, $\lambda_G = 0.2780$, 0.4989 from top to bottom. (b) The neutral curves of the GTW-(S)-modes ($n = 0$) in first-order approximation on the (ε,λ_0) plane for the cases of the concentration of impurity $C_\infty = 1.2$ mole%, $G_D = 140 \times 10^{-4}$ K/μm, and $V = 12,16,20$ μm/s, which correspond to the cases $\mathbb{M} = 0.9552$, $\kappa = 0.29$, and $G_c = 0.14485 \times 10^{-4}$, and $\varepsilon_c = 0.4666 \times 10^{-2}$, 0.5388×10^{-2}, 0.6024×10^{-2}; $\lambda_G = 0.6652$, 0.4989, 0.3991, from bottom to top.

(1) Symmetric modes: The tip's smoothness condition for these modes leads to

$$\mathrm{Re}[H(\varrho)]'(0) = \mathrm{Re}[H'(0)] = \mathrm{Re}\left[\frac{\mathrm{i}d_1}{\sqrt{\varepsilon}}\tilde{k}_0^{(1)}(0) + \frac{\mathrm{i}d_3}{\sqrt{\varepsilon}}\tilde{k}_0^{(3)}(0)\right] = 0. \quad (62)$$

Without loss of generality, we assume d_1 to be a positive real number and write $d_1 > 0$ and $d_3 = |d_3|e^{\mathrm{i}\chi_0\pi}$. Since for a real eigenvalue σ_0, $k_0^{(1)}(0)$ and $k_0^{(3)}(0)$ are both real. The tip's smoothness condition (62) for the S-mode becomes $\mathrm{Im}\{d_3\} = 0$. The connection condition for this case leads to

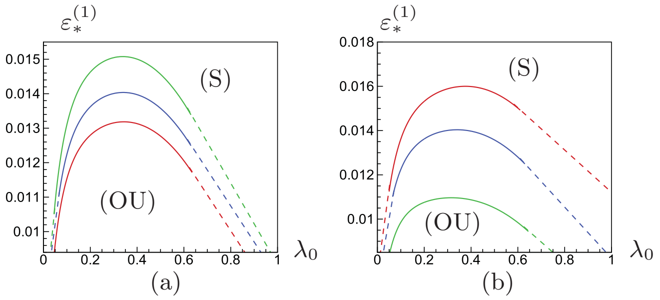

FIG. 12. (Color online) For the cases the temperature gradient $G_D = 140 \times 10^{-4}$ K/μm and $V = 16$ μm/s. (a) $\kappa = 0.29$, $\mathbb{M} = 0.0796$, 0.09552, 0.1194, which corresponding to $C_\infty = 1.0$, 1.2, 1.5 mole%, the neutral curves of the GTW-(S)-modes ($n = 0$) in first-order approximation on the (ε,λ_0) plane from bottom to top. (b) $\mathbb{M} = 0.0955$, $\kappa = 0.5$, 0.29, 0.1 the neutral curves of the GTW-(S)-modes ($n = 0$) in first-order approximation on the (ε,λ_0) plane from bottom to top.

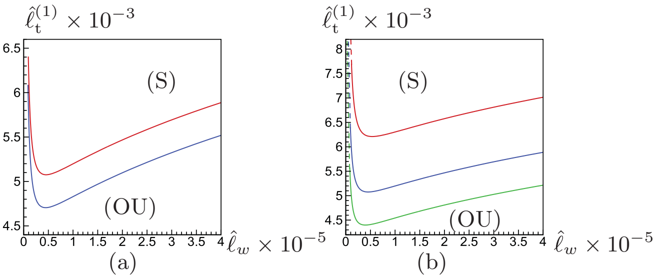

(a) (b)

FIG. 13. (Color online) (a) The neutral curves of the GTW-(S)-modes ($n = 0$) in first-order approximation on the $(\hat{\ell}_t,\hat{\ell}_w)$ plane for the cases of the concentration of impurity $C_\infty = 1.2$ mole%, the pulling velocity $V = 16\ \mu$m/s and various values of temperature gradient $G_D = 78 \times 10^{-4}$ K/μm, 140×10^{-4} K/μm, which corresponds to the cases: $\varepsilon_c = 0.5388 \times 10^{-2}$, $\mathbb{M} = 0.9552$, $\kappa = 0.29$, and $G_c = 0.8070 \times 10^{-5}$, 0.1448×10^{-4}, $\lambda_G = 0.2780$, 0.4989 from bottom to top. (b) The neutral curves of the GTW-(S)-modes ($n = 0$) in first-order approximation on the $(\hat{\ell}_t,\hat{\ell}_w)$ plane for the cases of the concentration of impurity $C_\infty = 1.2$ mole% $G_D = 140 \times 10^{-4}$ K/μm, and $V = 12, 16, 20\ \mu$m/s, which correspond to the cases $\mathbb{M} = 0.9552$, $\kappa = 0.29$, $G_c = 0.14485 \times 10^{-4}$, and $\varepsilon_c = 0.4666 \times 10^{-2}$, 0.5388×10^{-2}, 0.6024×10^{-2}; $\lambda_G = 0.6652, 0.4989, 0.3991$, from top to bottom.

$\frac{d_1}{d_3} = |\frac{d_1}{d_3}|e^{-i\chi_0\pi}, (\chi_0 = 0,1)$. As a consequence, we obtain the quantization condition:

$$\mathrm{Re}\left[\frac{1}{\sqrt{\varepsilon}}\int_0^{\varrho_c}\left(\tilde{k}_0^{(1)} - \tilde{k}_0^{(3)}\right)d\varrho\right] = \left(2n \pm \frac{1}{2}\right)\pi, \quad (n = 0,1,2,\ldots). \tag{63}$$

(2) Antisymmetric modes: The tip's smoothness condition for the antisymmetric modes is $\mathrm{Re}\{H(0)\} = \mathrm{Re}\{d_1 + d_3\} = 0$, which leads to $|\frac{d_1}{d_3}| = -\cos(\chi_0\pi) \leqslant 1$, hence $\frac{d_1}{d_3} = |\frac{d_1}{d_3}|e^{-i\chi_0\pi} = -\cos(\chi_0\pi)e^{-i\chi_0\pi}$, $(\chi_0 = 1 + \frac{1}{\pi}\cos^{-1}|\frac{d_1}{d_3}|)$. Thus, we obtain the quantization condition:

$$\mathrm{Re}\left\{\frac{1}{\sqrt{\varepsilon}}\int_0^{\varrho_c}\left(\tilde{k}_0^{(1)} - \tilde{k}_0^{(3)}\right)d\varrho\right\} = \left(2n + \frac{1}{2} + \chi_0\right)\pi, \quad (n = 0,1,2,\ldots). \tag{64}$$

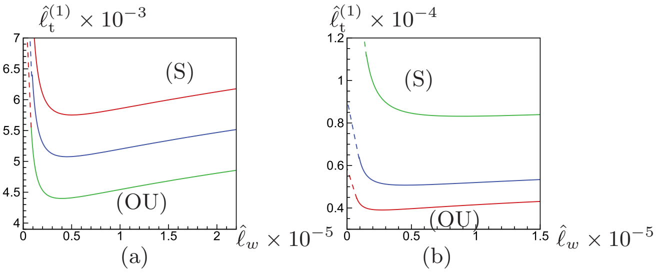

(a) (b)

FIG. 14. (Color online) For the cases the temperature gradient $G_D = 140 \times 10^{-4}$ K/μm and $V = 16\ \mu$m/s. (a) $\kappa = 0.29$, $\mathbb{M} = 0.0796$, 0.09552, 0.1194, which corresponding to $C_\infty = 1.0$, 1.2, 1.5 mole%, the neutral curves of the GTW-(S)-modes ($n = 0$) in first-order approximation on the $(\hat{\ell}_t,\hat{\ell}_w)$ plane from top to bottom. (b) $\mathbb{M} = 0.0955$, $\kappa = 0.5, 0.29, 0.1$ the neutral curves of the GTW-(S)-modes ($n = 0$) in first-order approximation on the $(\hat{\ell}_t,\hat{\ell}_w)$ plane from top to bottom.

The quantization condition (63) and (64) determine the eigenvalues σ_{0n} and the corresponding eigenfunction.

It is noted that due to $|\sigma_0| \ll 1$, one may derive an approximate form for the integrals involved in (63) and (64). From local dispersion relationship (27) and (28), one may derive the following asymptotic expansions for the wave-number functions k_e in the limit $\sigma_0 \to 0$:

$$\begin{aligned} k_e^{(3)} &= i(\varrho - i)\sigma_e + \cdots \\ k_e^{(1)} &= e^{-\frac{i\pi}{4}}(\varrho + i)^{\frac{3}{4}}(\varrho - i)^{\frac{1}{4}} - \tfrac{i}{2}(\varrho - i)\sigma_e + \cdots. \end{aligned} \tag{65}$$

Recalling that $k_e(\varrho) = \tilde{k}_0(\varrho)\dfrac{G(\varrho)}{\lambda_0\sqrt{\bar{\Lambda}_1}}$, we derive

$$\tilde{k}_0^{(1)}(\varrho) - \tilde{k}_0^{(3)}(\varrho) = \frac{2(1-\lambda_0)\sqrt{\bar{\Lambda}_1}}{\pi}\left[e^{-\frac{i\pi}{4}}\frac{(\varrho + i)^{\frac{3}{4}}(\varrho - i)^{\frac{1}{4}}}{(\varrho + ia)(\varrho - ia)} - \frac{3i}{2}\frac{(\varrho - i)}{(\varrho + ia)(\varrho - ia)}\sigma_e + \cdots\right].$$

To calculate the integral along the path $(\mathcal{C}) : \varrho = 0 \to -i$ contained in (63) and (64), one needs to separate two cases: A: $(0 < \lambda_0 < \frac{1}{2})$ and B: $(\frac{1}{2} < \lambda_0 < 1)$. It is found that the system does not have an eigenvalue for case A. Only case B is meaningful.

For case $(\frac{1}{2} < \lambda_0 < 1)$, we have $0 \leqslant a < 1$, the singular point $\varrho = -ia$ will be located in the middle of the path $(\mathcal{C})$. In this case one can calculate the integral as follows:

$$\begin{aligned} (\mathrm{I}) &= \int_0^{\varrho_c}\left[\tilde{k}_0^{(1)}(\varrho) - \tilde{k}_0^{(3)}(\varrho)\right]d\varrho \\ &= \left(\int_0^{-i(a-0)} + \int_{\mathcal{C}_r} + \int_{-i(a+0)}^{-i} + \int_{-i}^{\varrho_c}\right) \\ &\quad \times\left[\tilde{k}_0^{(1)}(\varrho) - \tilde{k}_0^{(3)}(\varrho)\right]d\varrho, \end{aligned}$$

where $(\mathcal{C}_r)$ is a semicircle centered at $\varrho = -ia$, connecting the points $\varrho = -i(a-0)$ and $\varrho = -i(a+0)$ in clockwise direction. As the result, we have

$$\begin{aligned} \mathrm{Re}\{\chi\} &= \frac{1}{\sqrt{\varepsilon}}\frac{(1-\lambda_0)\sqrt{\bar{\Lambda}_1}}{a}\left[(1-a)^{\frac{3}{4}}(1+a)^{\frac{1}{4}} - \frac{3}{2}(1+a)\sigma_e\right] \\ &= \frac{\sqrt{\bar{\Lambda}_1}}{\sqrt{\varepsilon}}\left[(2\lambda_0 - 1)^{\frac{3}{4}} - \frac{3}{2}\sigma_e\right], \end{aligned} \tag{66}$$

$$\mathrm{Im}\{\chi\} = \frac{2}{\sqrt{\varepsilon}}\frac{(1-\lambda_0)\sqrt{\bar{\Lambda}_1}}{a}\left[-\int_0^1\frac{(1-x)^{\frac{3}{4}}(1+x)^{\frac{1}{4}}}{(a-x)(a+x)}dx + \frac{3}{2}\int_0^1\frac{(1+x)}{(a-x)(a+x)}dx\right].$$

Based on these results, the following simplified quantization conditions are derived:

(1) For the S-modes,

$$\frac{3}{2}\sigma_e = \frac{3}{2}\frac{\bar{\Lambda}_0}{\sqrt{\bar{\Lambda}_1}}\sigma_0 = (2\lambda_0 - 1)^{\frac{3}{4}} - \sqrt{\frac{\varepsilon}{\bar{\Lambda}_1}}\left(n \pm \frac{1}{2}\right)\pi \quad (n = 0,1,2,\ldots). \tag{67}$$

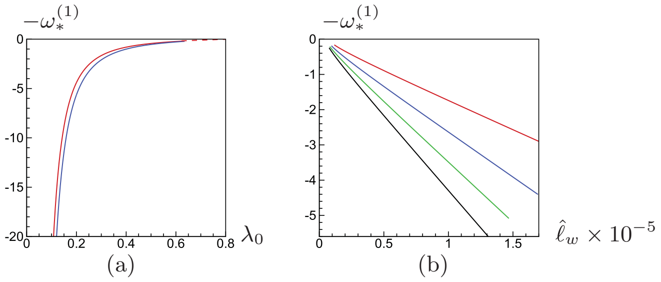

FIG. 15. (Color online) (a) For the cases of $V = 16\ \mu$m/s and $G_D = 78 \times 10^{-4}$ K/μm, 140×10^{-4} K/μm, the variations of eigenfrequency $\omega_*^{(1)}$ in first-order approximation with λ_0 from bottom to top. (b) For the cases of $G_D = 140 \times 10^{-4}$ K/μm and $V = 12, 16, 20, 24\ \mu$m/s, the variations of eigenfrequency $\omega_*^{(1)}$ in first-order approximation with $\hat{\ell}_w$ from top to bottom.

(2) For the A-modes,

$$\frac{3}{2}\sigma_e = \frac{3}{2}\frac{\bar{\Lambda}_0}{\sqrt{\bar{\Lambda}_1}}\sigma_0 = (2\lambda_0 - 1)^{\frac{3}{4}} - \sqrt{\frac{\varepsilon}{\bar{\Lambda}_1}}\left(2n + \frac{1}{2} + \chi_0\right)\pi \quad (n = 0,1,2,\ldots). \tag{68}$$

For any fixed ε and λ_0, from (67) or (68) one can obtain a discrete set of eigenvalues $\{\sigma_{0n}\}$ $(n = 0,1,2,3,\ldots)$. As a consequence, given λ_0, the system allows a discrete set of neutral stable modes ($\sigma_{0n} = 0$) corresponding to $\varepsilon = \varepsilon_n'$ $(n = 1,2,\ldots)$, where $\varepsilon_0' > \varepsilon_1' > \varepsilon_2' > \cdots > \varepsilon_n' > \cdots$. On the other hand, given $\varepsilon > 0$ the system allows a discrete set of neutral modes with width parameters $\lambda_0 = \lambda_{0n}$.

It is found that the neutral LF-A-mode is more stable than the neutral LF-S-mode with the same index n. The neutral LF-S-modes are determined by the formula:

$$\sqrt{\bar{\Lambda}_1}(2\lambda_0 - 1)^{\frac{3}{4}} = \sqrt{\varepsilon_*}\left(n + \frac{1}{2}\right)\pi, \quad \left(\frac{1}{2} \leqslant \lambda_0 < 1\right) \quad (n = 0,1,2,\ldots). \tag{69}$$

The form of (69) is again very similar to what we have obtained for the system of viscous fingering (see Refs. [34–37]). The neutral modes $(n = 0,1,2,\ldots)$ of LF instability yield a discrete set of steady arrayed cellular growth solutions.

We have calculated (67) and (69) under given operation parameters: $\{\varepsilon_c, G_c, \mathbb{M}\}$. The neutral curves for LF-S-modes $(n = 0,1,2)$ on the (λ_0,ε) and $(\hat{\ell}_w,\hat{\ell}_t)$ plane for the typical case $\varepsilon_c = 0.5388 \times 10^{-2}, \mathbb{M} = 0.9552 \times 10^{-1}, \kappa = 0.29, G_c = 0.14485 \times 10^{-4}, \lambda_G = 0.4989$ are shown in Fig. 16(a) and (b), respectively. It is seen that in the LF mechanism, the most dangerous mode is LF-S-mode with $(n = 0)$.

In Fig. 17 we show the neural curve of LF-S-mode $(n = 0)$ on the parameter $(\hat{\ell}_w,\varepsilon_c)$ plane for various λ_0. It is seen that as ε_c (or the pulling velocity V) increases, the primary spacing $\hat{\ell}_w$ decreases with a fixed λ_0. This is in agreement with the experimental observations.

It should be pointed that although the leading-order approximation of eigenvalues σ_0 are real numbers, but in the higher-order approximation, σ may be complex with a small imaginary part. Hence, the unstable LF modes may be slowly oscillating with a low frequency.

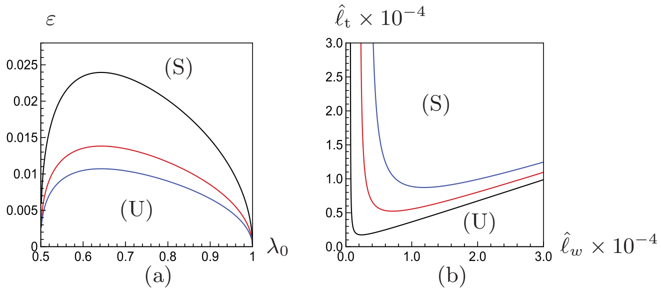

FIG. 16. (Color online) The neutral curves of the LF-(S)-modes $(n = 0,1,2)$ calculated by using the formula (67) in the corresponding parameter plane for the case $\varepsilon_c = 0.5388 \times 10^{-2}$, $\mathbb{M} = 0.9552 \times 10^{-1}$, $\kappa = 0.29$, $G_c = 0.14485 \times 10^{-4}$, $\lambda_G = 0.4989$. (a) In the (λ_0,ε) plane from top to bottom; (b) in the $(\hat{\ell}_w,\hat{\ell}_t)$ plane from bottom to top.

D. LF stability criterion and the global stability diagram of the system

The neutral curve of the LF-S-mode $(n = 0)$ shown in Fig. 16(a) can be called the fingerlike branch, as it has the range of the relative width $(0.5 < \lambda_0 < 1)$ and the smooth interface shape like the Saffman-Taylor fingers. Accordingly, the LF-S-modes may be called the fingerlike modes. Thus, the LF stability criterion or, e.g., the stability criterion of the fingerlike state can be described as follows:

$$\begin{array}{ll} (\varepsilon,\lambda_0); \quad (\hat{\ell}_t,\hat{\ell}_w) \in (S): & \text{stable} \\ (\varepsilon,\lambda_0); \quad (\hat{\ell}_t,\hat{\ell}_w) \in (U): & \text{unstable,} \\ & \text{nearly purely growing.} \end{array} \tag{70}$$

One may put the two neutral curves, LF-S-mode $(n = 0)$ and GTW-S $(n = 0)$ together on the (ε,λ_0) and $(\hat{\ell}_w,\hat{\ell}_t)$ parameter plane as shown in Fig. 18(a) and (b), respectively. Thus, we obtain the global stability diagrams of the system. It is proposed that the selected limiting state with steady, or nearly steady, periodic arrayed-cellular interface structure must be on the neutral curve of the LF-S-mode $(n = 0)$, whereas the selected oscillatory limiting state with an arrayed-dendritic interface structure must be on the neutral curve of the

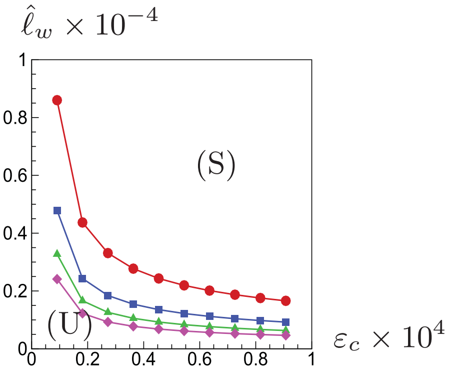

FIG. 17. (Color online) The neutral curves of the LF-(S) modes $(n = 0)$ on the parameter $(\hat{\ell}_w,\varepsilon_c)$ plane for the cases $G_D = 140 \times 10^{-4}$ K/μm, $\mathbb{M} = 0.09552$, $\kappa = 0.29$, $G_c = 0.1448 \times 10^{-4}$, and $\lambda_0 = 0.6, 0.7, 0.8, 0.9$ from top to bottom.

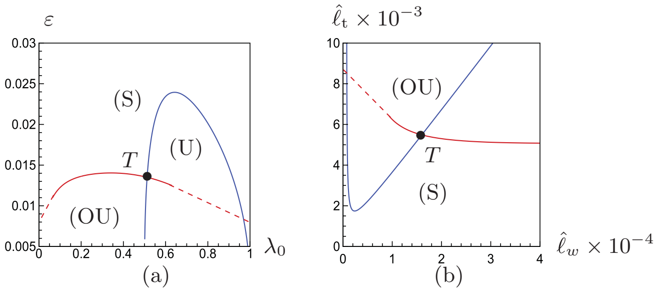

(a) (b)

FIG. 18. (Color online) The two neutral curves of S-modes ($n = 0$), which correspond to the LF stability and GTW stability, respectively, for the case $\varepsilon_c = 0.5388 \times 10^{-2}$, $\mathbb{M} = 0.9552 \times 10^{-1}$, $\kappa = 0.29$, $G_c = 0.14485 \times 10^{-4}$, $\lambda_G = 0.4989$. (a) In the (λ_0,ε) plane; (b) in the $(\hat{\ell}_w,\hat{\ell}_t)$ plane.

GTW-S-mode ($n = 0$). This selection condition for the limiting basic state may be called the *neutrally stable mode* (NSM) selection principle.

VII. SELECTION OF STEADY ARRAYED-CELLULAR GROWTH AND FINGERLIKE BRANCH OF NEUTRAL CURVES

For the model problem of fingerlike crystal growth in the channel with the fixed width ℓ_w, the dimensionless primary spacing $\hat{\ell}_w$ is a given constant. Thus, with the NSM selection principle the tip radius $\hat{\ell}_t$ as well as the whole basic state are fully determined from the fingerlike branch of the neutral curves. However, for the problem of deep arrayed-cellular growth in directional solidification, the imaginary side wall is not a realistic solid wall, but a free boundary. Hence, the primary spacing ℓ_w and the parameter $\hat{\ell}_w$ are undetermined. Thus, the NSM selection principle leads to a family of limiting states of a deep cellular growth system with various primary spacing parameter $\hat{\ell}_w$ under given growth conditions $(\varepsilon_c, G_c, \mathbb{M})$. In other words, there is no sharp selection for the system of cellular growth. The selection condition yields only a deterministic relationship between the tip radius and primary spacing. Our results support the argument previously proposed by experimentalists: The selected steady state solution depends on the history of growth [20] and are also consistent with the conclusions drawn by Unger-Brown and Ramprasad-Brown via the numerical simulations [21,22]. More recently, Pocheau *et al.* through their experiments confirmed that the primary spacing ℓ_w for the limited state was not uniquely determined by the operating conditions and the material properties; its value varies continuously within the available cell range, depending on the history of growth. Hence, Pocheau *et al.* treated the primary spacing ℓ_w as another independent control parameter for the cellular-array formation [25]. When the primary spacing ℓ_w is treated as an independent control parameter, like the width of channel in the above model problem, the selected steady periodic deep-cellular array at the late stage of growth is fully determined.

A. The comparisons with experimental data

In Fig. 19(a)–19(d) we show the neutral curves of LF modes in a $(\hat{\ell}_w,\hat{\ell}_t)$ plane under typical growth conditions.

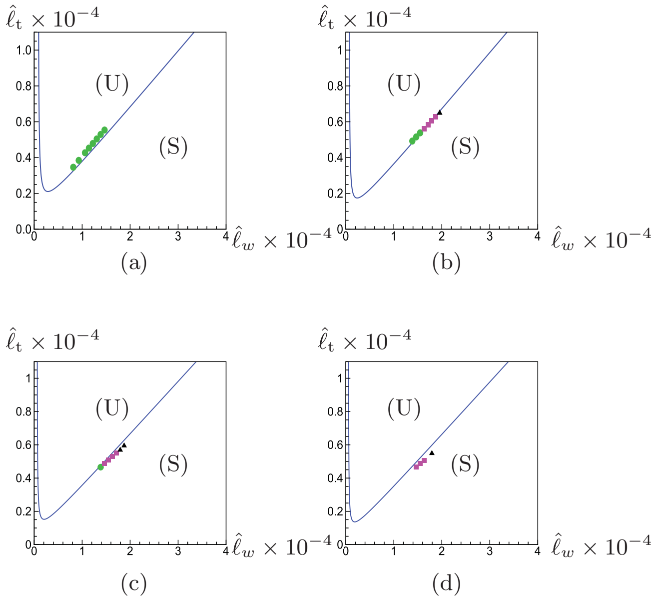

(a) (b) (c) (d)

FIG. 19. (Color online) The selected cellular array growth for the case $G_D = 140.0 \times 10^{-4}$ K/(μm), $\kappa = 0.29$, $\mathbb{M} = 0.8432 \times 10^{-1}$, and (a) $V = 12$ μm/s; (b) $V = 16$ μm/s; (c) $V = 20$ μm/s; (d) $V = 24$ μm/s. Here, to eliminate the three-dimensional effect occurring in the experiments, we have chosen $\tilde{\ell}_c = 1.3\ell_c$ as the length scaling for the experimental data [25].

The experimental data for the limiting states for these cases measured by Pocheau *et al.* are also included in these figures for the comparisons. The thermodynamic parameters adopted in the calculations are shown in Table I.

Note that the parameter of thickness $\delta/\ell_c = 2.12 \times 10^4$ μm is (4–10) larger than the parameter of tip radius. Hence, there is a significant three-dimensional effect included in the experiments. Moreover, the data of tip radius ℓ_t measured in the experiments is only one principal tip radius on (x,y) plane, the second principal radius along the thickness is omitted. As a consequence, with these data the effect of tip mean curvature reflected in the Gibbs-Thomson formula is greatly underestimated. To convert the three-dimensional experimental system to an equivalent two-dimensional model system for the comparison with the two-dimensional theory, one must compensate such an underestimation by setting a bigger effective two-dimensional surface tension coefficient

TABLE I. Thermodynamic data used in the calculations for the nominally pure SCN system used by Pocheau *et al.* ([25,27]) in the cell of growth with thickness $\delta = 50$ μm, width 45 mm, and length 150 mm.

κ_D	1.30×10^{-5} cm^2 s^{-1}
κ	0.29
m	1.9 K mol%$^{-1}$
c_∞	1.2 mol%
δ/ℓ_c	2.12×10^4 μm
ℓ_c	0.2359×10^{-2} μm
c_p	0.4630 cal g^{-1} K^{-1}
mol	80.092 g/mol
ΔH	11.051 cal/mol

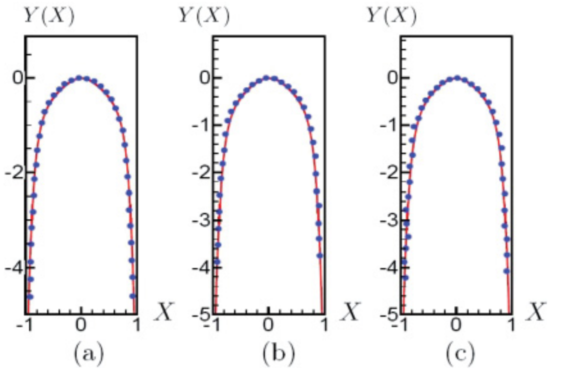

FIG. 20. (Color online) The interface shapes selected at the late stage of growth for the typical case $G_D = 140.0 \times 10^{-4}$ K/(μm), $V = 20\ \mu$m/s, $\kappa = 0.29$, $\mathbb{M} = 0.8432 \times 10^{-1}$, and (a) $\ell_w = 65.0\ \mu$m; (b) $\ell_w = 62.5\ \mu$m; (c) $\ell_w = 60.0\ \mu$m. The dots are experimental data given by Pocheau *et al.* [25].

with a factor $f_c > 1$ for the two-dimensional model of the experimental system. Here, we set $f_c = 1.3$ in the calculations. Pocheau *et al.* ([25]) classify the growth states observed in their experiments into the three categories based on the amplitudes of oscillation of their interface shape: steady states, weakly dendritic states, and moderate dendritic states. We marked these data in the figures with different symbols: full circles, squares, and triangles, respectively.

It is seen from Fig. 19(a)–19(d) that the experimental points are quite close to the LF neutral curves. The discrepancies between theory and experiments are systematic and fall in the range of the experimental measurements errors, 10%–20%. In Fig. 20(a)–23(c) we show the interface shapes predicted by the theory and compared with the experimental data under the same growth conditions. The quantitative agreements between both are excellent.

Hence, it is concluded that the theoretical results are in a very good quantitative agreement with these experiments' data. The systematical discrepancy may be induced by the physical effects, including the effects of three-dimensional geometry, the anisotropy of surface tension, and interface kinetics that the theoretical model are neglected.

VIII. SELECTION OF ARRAYED-DENDRITIC GROWTH AND NEEDLELIKE BRANCH OF NEUTRAL CURVES

The global GTW neutral state that we found describes a perfect, periodic, oscillatory, dendritic array with infinitesimal magnitude, which has a fixed relative width λ_0 and selected $\varepsilon = \varepsilon_*$, accordingly, a fixed primary width and tip location. However, it has an oscillating tip radius and dendritelike interface shape. Hence, one may call the neutral curve of GTW modes the dendritelike branch, and GTW wave modes the dendritelike modes. The distribution of amplitude of oscillation along the interface is described by the eigenfunction of a neutral mode in the linear theory up to an arbitrary constant factor, whereas the frequency of oscillation along its whole interface is the constant determined by the imaginary part of eigenvalue ω_*. In the nonlinear regime, these global GTW neutral modes develop into the limit circles with small but finite characteristic magnitude, whose location on the parameters $(\hat{\ell}_w, \hat{\ell}_t)$ plane must be close to the GTW neutral curve. The selected oscillatory dendritic array growth observed in the experiments is just described by this nonlinear limit circle. Thus, the *neutral stable mode* (NSM) selection principle can be justified.

A. The origin of side branching and wave reflections and amplification due to the GTW mechanism

The GTW stability mechanism discovered in the system under study is quite similar to that found in free dendritic growth. As it is well known, based on the global stability theory the interfacial wave (IFW) theory of free dendritic growth not only yields the selection condition for a free single dendritic growth, but also reveals well the origin and essence of the side branching over the interface [37–42]. The GTW mechanism now works for the system of directional solidification as well. As shown by (48), in the W-wave representation, a perturbed state can be described in the form $\tilde{W}_0(\varrho) = D_1[\tilde{W}_0^{(+)}(\varrho) - \mathrm{i}\tilde{\mathrm{W}}_0^{(-)}(\varrho)]$, where $\tilde{W}_0^{(+)}$ is the outgoing wave toward the root, while $\tilde{W}_0^{(-)}$ is the incoming wave toward the tip propagating along the interface. In the segment of interface $(\rho_c' < \rho < \infty)$, the perturbation state is described in the form $\tilde{W}_0(\varrho) = \tilde{W}_0^{(T)}(\varrho)$, which is the incoming wave propagating along the interface from the root toward the tip. The global wave diagram of the system is sketched in Fig. 21. It reveals that, under the action of the incoming wave from the root $\tilde{W}_0^{(T)}(\varrho)$, an outgoing wave $\tilde{W}_0^{(+)}(\varrho)$ is fully reflected at the point ρ_c' with the reflection rate $R = |D_1/D_3| = 1$ and becomes the incoming wave $\tilde{W}_0^{(-)}(\varrho)$. The incoming wave $\tilde{W}_0^{(-)}(\varrho)$ is subsequently fully reflected at the cell's tip and becomes the outgoing wave $\tilde{W}_0^{(+)}(\varrho)$. During this course the perturbed state is amplified. the amplification rate is the real part of the eigenvalue, σ_R, determined by the quantization condition (59).

It is concluded that the origin and essence of the side branching along the cellular interface, is the presence of a discrete set of the unstable oscillatory GTW wave modes generated by the wave diagram involving the reflections and amplification of the interfacial waves. This mechanism was called the *global trapped wave* (GTW) mechanism in the IFW theory.

In some region of the parameters $(\hat{\ell}_w, \hat{\ell}_t)$ plane, the smooth steady cellular growth is observable, because in that region all GTW unstable modes are decaying. In the other region of

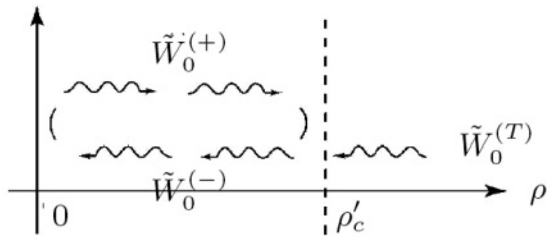

FIG. 21. Wave diagram of the GTW mechanism.

$(\hat{\ell}_w,\hat{\ell}_t)$ plane, where the system permits a finite number of growing GTW modes, the side branches are observable and self-sustaining without any external enforced stimulations.

These conclusions are well verified by the experimental observations, as well as the numerical simulations qualitatively as demonstrated below. Both the experiments by Georgelin and Pocheau [27] and the numerical simulation by Echebarria, Karma, and Gurevich (EKG) [30] show that the frequency of the observed oscillation at the interface with side branching is independent of the distance behind the tip. This verifies the conclusion of the IFW theory that the frequency of oscillation is an eigenfrequency of the system. The GP experiments show that the amplitudes of oscillation at different points of interface have the cross-correlation, which is consistent with the IFW theory that the distribution of the oscillatory amplitude of interface is mainly described by the eigenfunction of the GTW mode ($n = 0$).

In particular, Echebarria *et al.* calculate the power spectrum of side-branching oscillation for a typical case of arrayed dendritic growth. They found that there are a sequence of peaks in the figure [see Fig. 16(b) in Ref. [30]]. These peaks can be considered as strong evidence of the existence of the eigenfrequency ω_* of the GTW-S-mode ($n = 0$) in the system. Indeed, according to the well-known linear resonance theory, a dynamical system with eigenfrequency ω_* may have the resonances with an external weak force oscillating with the eigenfrequency ω_* or the corresponding period $T_* = 2\pi/\omega_*$, such resonance appears as the highest peak in the power spectrum and is called the primary harmonic resonance. Moreover, the system may allow a sequence of subharmonic resonances with the external weak oscillatory forces with periods $T_*/2, T_*/3, \ldots$, as well as the superharmonic resonances at the periods $2T_*, 3T_*, \ldots$. These resonances will appear as the peaks located at $T_*/2, T_*/3, \ldots$ and $2T_*, 3T_*, \ldots$ with decreasing heights in the power spectrum.

To confirm the nature of side-branching oscillation further, we make a quantitative comparison between the results of numerical simulations and theoretical prediction as below. The EKG's numerical simulation was for the case $V = 32\mu$m/s, $G_{\mathrm{D}} = 140$ K/cm, and primary spacing $\ell_w = 138.9$ μm and for the impure succinonitrile (SCN) alloy system with anisotropy of surface tension $\epsilon_4 = 0.007$. The peak is found for the period $T = T_0 = 0.94$ s. We calculate the neutral GTW-S modes in terms of the theory developed in the present paper for the same case and the same system and derive the critical number of the stability parameter ε_*, as well as the eigenfrequency ω_*. Note that the numerical simulations by EKG were based on the phase field model, whose parameters' setting involves some uncertainties. For instance, with their notations, they set the ratio parameter $\epsilon = W/D_0 = 36$–72 associated with the thickness of interface layer and the coupling constant $\lambda = 32$–64. The choices of these constants, of course, may more or less affect the numerical value of T_0. Moreover, as estimated by EKG, their numerical results have 10% error. On the other hand, the analytical theory neglected the effect of anisotropy of surface tension. As a consequence, there will be a systematic discrepancy between the numerical simulations and analytical theory. Hence, to compare the numerical results of asymptotic theory with the numerical simulations, one needs to modify the critical value of stability parameter ε_* obtained from asymptotic theory by introducing a proper multiplier f_c. We find that, with $f_c = 1.305$, the zeroth-approximation of the neural GTW-S- ($n = 0$) mode yields the eigenperiod $T_* = 0.940$ s, the same as T_0 that calculated by the EKG numerical simulation, whereas with $f_c = 1.583$ the first-order approximation of the neural GTW-S ($n = 0$) mode yields the eigenperiod $T_* = T_0 = 0.940$ s. The above values of the factor f_c are apparently in a reasonable range.

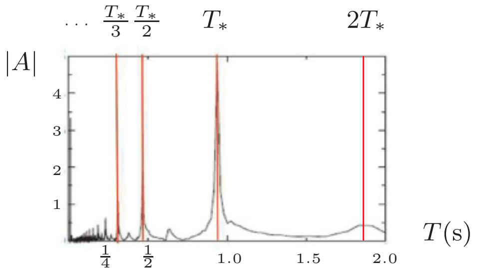

FIG. 22. (Color online) Power spectrum and the resonances of the system of arrayed-cellular growth with external perturbations.

We mark all the resonance periods $2T_*, T_*, T_*/2, T_*/3, \ldots$ with solid lines in the figure of the power spectrum given by Echebarria *et al.* ([30]) as shown in Fig. 22. It is seen that the peaks of the power spectrum curve are all respectively located at the places very close to these lines, in full agreement with the assessment made by the IFW theory.

In the region on the $(\hat{\ell}_w,\hat{\ell}_t)$ plane, where all the GTW modes are decaying, as indicated above, the system remains with the steady arrayed-cellular interface. However, in that region, the side branches can be generated by continuously applying sufficiently strong external perturbations or noise. This is because not only neutrally stable GTW mode but also the GTW modes with small decaying rate can be activated by the sufficiently strong external oscillatory perturbations as some inhomogeneous force terms in the dynamic system. However, the characteristics of these artificial side branches are qualitatively different from those observed in GTW unstable region. The characteristic amplitude of such side branches will depend on and are proportional to the strength of the perturbations; the dendritic patterns will disappear with time exponentially, once the external forces stop. These features are precisely what are observed in EKG numerical simulations.

It should be indicated that the above assessments by the IFW theory on the origin and essence of side-branching structure were systematically demonstrated in 1990s, through a series of articles and monographs (see Refs. [37–41]); these theoretical predictions have been compared with and verified by a number of previous experiments for the systems of free dendritic growth (see Refs. [42,43]). Now for the systems of directional solidification, these assessments are further confirmed by the GP experiments and the EKG numerical simulations.

B. Comments on the so-called noise selected amplification mechanism

The paper by Echebarria *et al.*, like those ofother researchers, continues using the so-called noise selected amplification mechanism for explaining the origin of side branchings on the interface [30]. This effort originated from the attempt to resolve the contradiction of the microscopic solvability condition (MSC) theory with the experimental observations of free dendritic growth. According to the MSC theory, a system cannot allow dendritic growth without the presence of the anisotropy of surface tension; with a small amount of the anisotropy of surface tension the system will allow a discrete set of smooth needlelike growths with no side branching. Such a statement obviously contradicts the experimental observations, which indicate that growing dendrite always has side branching. To offset the defect of the MSC theory, “the noise selected amplification (NSA) mechanism” as an addition to the MSC theory was proposed by some researchers early on. The NSA states that the side branching is due to the continuous presence of noise in the system, namely, no continuously added noise, no side branching; furthermore, the noise with selected frequency can be amplified somehow, and this results in the side branchings. Note that such an NSA mechanism does not really clarify the origin and essence of the side branching. It provides no solutions for the questions, such as what is the nature and numerical value of the frequency that is to be amplified? How many such frequencies the system allows? What is the rate of amplification? etc. All these questions, as we have pointed out, can be resolved in terms of the GTW mechanism in the IFW theory.

In attempting to demonstrate the NSA mechanism, Echebarria *et al.* in their paper ([30]) proposed that there may exist a feedback process in the system. However, without the aid of the IFW theory and GTW mechanism, they still cannot clarify the nature and origin of such feedback with the clear answers to the questions, as to what is the cause of feedback, what portion of signal was fed back, where the feedback started, etc.

As the matter of fact, according to the GTW mechanism, the feedback is generated not only due to the signal $\tilde{W}^{(T)}$ propagating from the root toward the tip, but also due to the reflection of the outgoing wave $\tilde{W}^{(+)}$ from the tip at a certain point ξ_c on the interface of the basic state. It is regrettable that, for so many years after the publication of the IFW theory and GTW mechanism, Echebarria *et al.* ignored this theory in their numerical investigation on the dynamics of side branching, despite the fact that it was quite applicable to the subject under their discussion.

IX. TRANSITION FROM CELLULAR ARRAY TO DENDRITIC ARRAY

We now put the experimental data obtained by Pocheau *et al.* ([25]) in the stability diagram as shown in Fig. 23(a)–23(d). It is seen that the data representing steady smooth cellular arrays all stay outside the oscillatory unstable region (OU); whereas the data with the interfacial dynamical activities, such as the weak oscillations and the bursts of side branching over the interface, all fall in the OU. This situation further confirm the presence of the unstable GTW modes in the system. The experimental data given by Pocheau *et al.* (2006) does not consider the cases of the strong dendritic array. We expect that the data for the strong, periodic arrayed dendritic growth with $\hat{\ell}_w \gg 1$ will be located near the dendritelike branch in the global stability diagram, since the arrayed-dendritic growth reduces to single dendritic growth when $\ell_w \to \infty$.

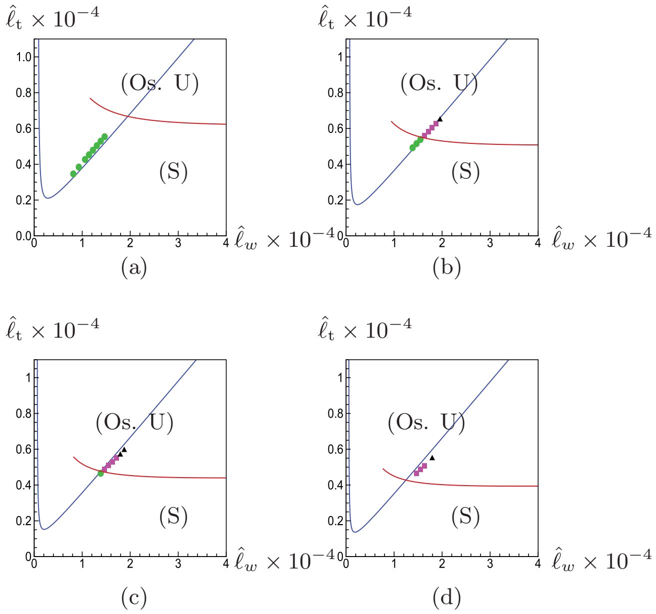

(a) (b)

(c) (d)

FIG. 23. (Color online) The selected cellular array growth for the case $G_D = 140.0 \times 10^{-4}$ K/(μm), $\kappa = 0.29$, $\mathbb{M} = 0.8432 \times 10^{-1}$, and (a) $V = 12$ μm/s; (b) $V = 16$ μm/s; (c) $V = 20$ μm/s; (d) $V = 24$ μm/s. In the experimental data, the full circles represent the steady cellular array, the squares represent weakly oscillatory cellular array, and the triangles represent the moderate oscillatory cellular array.

It is also noted that the data with the weak and moderate interfacial dynamical activities are slightly off the LF neutral curve, but remain nearby, not close to the dendritelike branch. This is still a not fully resolved puzzle for us. A simple explanation for these experimental results is that the systems were still in the transient states. The experimental time for these cases was not long enough, for the interface shapes to have evolved into a periodic deep-dendritic array.

There may be another possibility. As the effects of the anisotropy of surface tension and the interface kinetics are neglected in the current two-dimensional model, some global stability mechanisms of the system might be missed. One may presume that with the inclusion of these physical effects, the single GTW neutral curve found in a two-dimensional simplified model might bifurcate into two new branches. It might be for this reason that the global stability diagram derived in the present paper does not yield the hysteresis suggested by the numerical simulations by Echebarria *et al.* [30]. To confirm such a hysteresis mechanism, further analytical investigations with more realistic models and experimental work are needed.

X. CONCLUDING REMARKS

The present paper investigates the global instability mechanisms and selection criterion of steady deep arrayed-cellular growth in directional solidification. We have resolved the eigenvalue problem for the linear perturbed states in terms of a multiple-variable expansion method and obtained the global-modes solutions and the quantization conditions for the corresponding eigenvalues σ. It is found that the stability mechanisms of directional solidification have profound similarities with that of viscous fingering and free dendritic growth [34–36], [37–41]. On the basis of the global stability mechanisms, the neutral-mode selection principle for the limiting state of growth is proposed and the origin and essence of side branching is explored. It is concluded that the effect of anisotropy of surface tension is not essential for the selection of steady arrayed cellular growth and the origin of side branching.

The global stability theory established in the present paper is predictive. The theoretical results of the stability criterion ε_*, the eigenfrequencies, ω_*, the pattern-transition point T in the parameter plane, etc., are all verifiable with the experimental data under given growth conditions. The comparisons of theoretical results with the most recent experimental works by Pocheau *et al.* ([25–27]) as well as the most recent numerical simulations by Gurevich *et al.* and Echebarria *et al.* [30] have shown very good quantitative agreements.

The main results are summarized as follows:

(1) It is found that the system has two discrete spectra of eigenvalues corresponding to the quantum numbers ($n = 0,1,2,\ldots$): the complex spectrum with $|\sigma| = O(1)$ and the nearly real spectrum with $|\sigma| \ll 1$. Accordingly the system involves two types of instability mechanisms: the global traveling wave (GTW) instability, whose neutral modes yield strong oscillatory fingers, and the low-frequency (LF) instability, whose neutral modes yield steady smooth or weakly oscillatory fingers. Among the all GTW modes, the symmetric GTW-S-mode with $n = 0$ is the most dangerous oscillatory mode, while among the all LF modes, the symmetric LF-S-mode with $n = 0$ is the most dangerous nearly steady or weakly oscillatory mode.

(2) The neutral curves of the GTW-S-mode ($n = 0$) and LF-S ($n = 0$) divide the parameter (ε,λ_0) plane (and $(\hat{\ell}_w,\hat{\ell}_t)$ plane into two subdomains: the stable domain and unstable domain. The *neutrally stable mode* (NSM) selection principle suggests that under given growth conditions the fully developed limiting solution is selected on the two segments of neutral curves of the GTW-S-mode with $n = 0$ and LF-S-mode with $n = 0$, which intersect with each other at the point T as shown in Fig. 18.

(3) The origin and essence of the side branching in directional solidification are the same as that in free dendritic growth, due to the GTW mechanism that involves wave reflection and amplification along the interface. The side-branching structure on the interface is self-sustaining and can persist without continuously applying the external perturbations or noise.

(4) Under our two-dimensional model, the sharp selection of the limiting state needs another geometric constraint, such as the width of the growth channel for the problem of fingerlike crystal growth in a channel. Without an additional length scale, in the system of two-dimensional cellular growth, the limiting state selected by the NSM principle is not unique, the selection criterion yields a deterministic relationship between the tip radius ℓ_t and primary spacing ℓ_w, and the primary spacing itself may vary depending on the history of growth.

ACKNOWLEDGMENTS

The work is supported by Nankai University, China, and partial support is from the University of Science and Technology in Beijing under the Overseas Distinguished Scholar program sponsored by the Department of Chinese Education. The authors are very grateful to S. H. Davis for his valuable suggestions and discussions.

APPENDIX

A. Derivation of the first-order approximate solution and singular point

The equation for the first-order approximation can be obtained from (9) as the following:

$$\left(k_0^2+g_0^2\right)\left(\frac{\partial^2}{\partial\xi_+^2}+\frac{\partial^2}{\partial\eta_+^2}\right)\tilde{C}_1 = a_0(\xi,\eta)\mathrm{e}^{\mathrm{i}\xi_+-\eta_+}, \tag{A1}$$

where

$$a_0 = 2(k_0-\mathrm{i}g_0)\left(\frac{\partial A_0}{\partial\eta}-\mathrm{i}\frac{\partial A_0}{\partial\xi}\right). \tag{A2}$$

To eliminate the secular terms on the right-hand side of (A1), one must set $a_0 = 0$. Then from (A2) it follows that

$$\left(\frac{\partial}{\partial\eta}-\mathrm{i}\frac{\partial}{\partial\xi}\right)A_0(\xi,\eta) = 0. \tag{A3}$$

Equation (A3) is a first-order hyperbolic equation. $A_0(\xi,\eta)$ can be solved in the ξ-η plane as an initial value problem given the initial conditions on the line $\eta = 0$:

$$A_0(\xi,0)=\hat{A}_0(\xi)=-\left[W\hat{\mathrm{Pe}}(\lambda_{\mathrm{G}}-y_{*0}+1)+\frac{\bar{k}_0^2}{\mathbb{M}W\mathcal{G}_0(\xi)}\right]\hat{D}_0.$$

We then derive that at $\eta = 0$,

$$\hat{D}_0Q_0 = \frac{\partial}{\partial\eta}A_0(\xi,\eta)\bigg|_{\eta=0} = -\mathrm{i}\hat{D}_0\frac{\partial}{\partial\xi}\left[\frac{\bar{k}_0^2}{\mathbb{M}W\mathcal{G}_0(\xi)}\right]. \tag{A4}$$

These formulas will be needed later to solve for $k_1(\xi)$.

We now turn to solve the governing equation of $\tilde{C}_1$:

$$\left(\frac{\partial^2}{\partial\xi_+^2}+\frac{\partial^2}{\partial\eta_+^2}\right)\tilde{C}_1 = 0. \tag{A5}$$

The corresponding interface conditions are: at the interface $\eta_+ = 0, \eta = 0$:

$$\tilde{C}_1 + W\hat{\mathrm{Pe}}(\lambda_{\mathrm{G}}-y_{*0}+1)\tilde{h}_1 - \frac{\bar{k}_0^2}{\mathbb{M}W\mathcal{G}_0(\xi)}\frac{\partial^2\tilde{h}_1}{\partial\xi_+^2} = \frac{2\bar{k}_0\bar{k}_1}{\mathbb{M}W\mathcal{G}_0(\xi)}\frac{\partial^2\tilde{h}_0}{\partial\xi_+^2} - h_1\bar{k}_0\frac{\partial\tilde{C}_0}{\partial\eta_+}, \tag{A6}$$

and

$$\begin{aligned}&\bar{k}_0\frac{\partial\tilde{C}_1}{\partial\eta_+}+\sigma_0W\hat{\mathrm{P}}\mathrm{e}(1-\kappa)y_{*0}\mathcal{G}_0^2(\xi)\tilde{h}_1+\bar{k}_0W\hat{\mathrm{P}}\mathrm{e}\\&\times[\lambda_\mathrm{G}-(1-\kappa)y_{*0}]Y_{\xi,0}(\xi)\frac{\partial\tilde{h}_1}{\partial\xi_+}\\=&-\frac{\partial\tilde{C}_0}{\partial\eta}-h_1\bar{k}_0^2\frac{\partial^2\tilde{C}_0}{\partial\eta_+^2}-\bar{k}_1\frac{\partial\tilde{C}_0}{\partial\eta_+}\\&-W\hat{\mathrm{P}}\mathrm{e}\lambda_GY_{\xi,0}(\xi)\bar{k}_1\frac{\partial\tilde{h}_0}{\partial\xi_+}\\&+W\hat{\mathrm{P}}\mathrm{e}[\lambda_\mathrm{G}-(1-\kappa)y_{*0})]Y_{\eta\eta}(\xi,0)\tilde{h}_0\\&-\sigma_1W\hat{\mathrm{P}}\mathrm{e}(1-\kappa)y_{*0}\mathcal{G}_0^2(\xi)\tilde{h}_0\\&+\bar{k}_1W\hat{\mathrm{P}}\mathrm{e}(1-\kappa)y_{*0}Y_{\xi,0}(\xi)\frac{\partial\tilde{h}_0}{\partial\xi_+}.\end{aligned}\tag{A7}$$

This first-order approximate system is inhomogeneous, which allows the form of normal modes solutions:

$$\begin{aligned}\tilde{C}_1&=A_1(\xi,\eta)\exp[\mathrm{i}\xi_+-\eta_+],\\\tilde{h}_1&=\hat{D}_1\exp[\mathrm{i}\xi_+],\end{aligned}\tag{A8}$$

and is subject to the solvability condition:

$$I_2+\bar{k}_0I_1=0,\tag{A9}$$

where

$$\begin{aligned}I_1=&-\frac{2\bar{k}_0\bar{k}_1}{\mathbb{M}W\mathcal{G}_0(\xi)}+h_1(\xi)\bar{k}_0\bigg[-W\hat{\mathrm{P}}\mathrm{e}(\lambda_\mathrm{G}-y_{*0}+1)\\&-\frac{\bar{k}_0^2}{\mathbb{M}W\mathcal{G}_0(\xi)}\bigg]\end{aligned}$$

and

$$\begin{aligned}I_2=&-Q_0+h_1(\xi)\bar{k}_0^2\left[W\hat{\mathrm{P}}\mathrm{e}(\lambda_\mathrm{G}-y_{*0}+1)+\frac{\bar{k}_0^2}{\mathbb{M}W\mathcal{G}_0(\xi)}\right]\\&-\bar{k}_1\bigg[W\hat{\mathrm{P}}\mathrm{e}(\lambda_\mathrm{G}-y_{*0}+1)+\frac{\bar{k}_0^2}{\mathbb{M}W\mathcal{G}_0(\xi)}\\&+\mathrm{i}W\hat{\mathrm{P}}\mathrm{e}\lambda_GY_{\xi,0}(\xi)\bigg]+\mathrm{i}\bar{k}_1W\hat{\mathrm{P}}\mathrm{e}(1-\kappa)y_{*0}Y_{\xi,0}(\xi)\\&+W\hat{\mathrm{P}}\mathrm{e}[\lambda_\mathrm{G}-(1-\kappa)y_{*0})]Y_{\eta\eta}(\xi,0)\\&-\sigma_1W\hat{\mathrm{P}}\mathrm{e}(1-\kappa)y_{*0}\mathcal{G}_0^2(\xi).\end{aligned}$$

The formula (A9) leads to

$$\begin{aligned}\bar{k}_1=&\frac{1}{F(\xi)}\bigg\{-W\hat{\mathrm{P}}\mathrm{e}[\lambda_\mathrm{G}-(1-\kappa)y_{*0})]Y_{\eta\eta}(\xi,0)\\&-\mathrm{i}\frac{\partial}{\partial\xi}\left[\frac{\bar{k}_0^2}{\mathbb{M}W\mathcal{G}_0(\xi)}\right]+\sigma_1W\hat{\mathrm{P}}\mathrm{e}(1-\kappa)y_{*0}\mathcal{G}_0^2(\xi)\bigg\},\end{aligned}\tag{A10}$$

where we have defined

$$F(\xi)=F_0(\xi)-\frac{3\bar{k}_0^2}{\mathbb{M}W\mathcal{G}_0(\xi)}\tag{A11}$$

and

$$\begin{aligned}F_0(\xi)=&-W\hat{\mathrm{P}}\mathrm{e}(\lambda_\mathrm{G}-y_{*0}+1)+\mathrm{i}W\hat{\mathrm{P}}\mathrm{e}\\&\times[(1-\kappa)y_{*0}-\lambda_\mathrm{G}]Y_{\xi,0}(\xi).\end{aligned}\tag{A12}$$

It is noted from (A10) that the first-order approximate solution $\bar{k}_1(\xi)$ has the singularity at the roots of function $F(\xi)$, which are located in the extended complex ξ plane: $\zeta=\xi+\mathrm{i}\xi_\mathrm{I}$.

B. The extended complex ζ plane and the location of the singular point

To identify the singularity of the MVE solution, one needs to extend all the functions such as $F(\xi)$, $\bar{k}_0(\xi)$, $Y_{\xi,0}(\xi)$, $\mathcal{G}_0(\xi)$, etc., by the analytical continuation, to the corresponding complex functions $F(\zeta)$, $\bar{k}_0(\zeta)$, $Y_{\zeta,0}(\zeta)$, $\mathcal{G}_0(\zeta)$, etc., in the complex plane $\zeta=\xi+\mathrm{i}\xi_\mathrm{I}$. Meanwhile, the function $\tilde{k}_0(\rho)$ is extended by the analytical continuation to the complex function $\tilde{k}_0(\varrho)$ in the complex plane $\varrho=\rho+\mathrm{i}\rho_\mathrm{I}$. Moreover, one needs to consider the solutions $\tilde{C}(\xi,\eta)$, $k(\xi,\eta)$, $\phi(\xi,\eta)$ and $\psi(\xi,\eta)$ in the extended (ζ,η) space.

It is deduced that after the analytical continuation, the wave-number function $\bar{k}_0(\zeta)\equiv\{\bar{k}_0^{(1)}(\zeta),\bar{k}_0^{(2)}(\zeta),\bar{k}_0^{(3)}(\zeta)\}$ is subject to the following extended dispersion formula:

$$\sigma_0=\Sigma(\bar{k}_0,\zeta)=\frac{\bar{k}_0}{\bar{\Lambda}_0\mathcal{G}_0^2(\zeta)}\left\{[\lambda_0+\mathrm{i}Y_{\zeta,0}(\zeta)]-\frac{\bar{k}_0^2}{\bar{\Lambda}_1\mathcal{G}_0(\zeta)}\right\}.\tag{A13}$$

Accordingly, the analytical function $\tilde{k}_0(\varrho)\equiv\{\tilde{k}_0^{(1)}(\varrho),\tilde{k}_0^{(2)}(\varrho),\tilde{k}_0^{(3)}(\varrho)\}$ is subject to the extended dispersion formula:

$$\sigma_0=\frac{G(\varrho)\tilde{k}_0}{\bar{\Lambda}_0\lambda_0S^2(\varrho)}\left[(1-\mathrm{i}\varrho)-\frac{G^2(\varrho)\tilde{k}_0^2}{\bar{\Lambda}_1\lambda_0^2S(\varrho)}\right]\tag{A14}$$

or

$$\sigma_\mathrm{e}=\Sigma(k_\mathrm{e},\varrho)=\frac{k_\mathrm{e}}{S^2(\varrho)}\left[(1-\mathrm{i}\varrho)-\frac{k_\mathrm{e}^2}{S(\varrho)}\right].\tag{A15}$$

It may be derived from the extended dispersion formula (A13) that

$$\frac{\partial\Sigma(\bar{k}_0,\zeta)}{\partial\bar{k}_0}=\frac{F(\zeta)}{W\hat{\mathrm{P}}\mathrm{e}(1-\kappa)y_{*0}\mathcal{G}_0^2(\zeta)}.\tag{A16}$$

It follows from the above that at the singular point $F(\zeta_c)=0$ we have

$$\frac{\partial\Sigma(\bar{k}_0,\zeta_c)}{\partial\bar{k}_0}=0\quad\text{and}\quad\left[\bar{k}_0^{(1)}(\zeta_c)-\bar{k}_0^{(3)}(\zeta_c)\right]=0.\tag{A17}$$

Combining (A17) and (A13), we derive that

$$\sigma_0=\frac{2}{\sqrt{27}}\frac{\sqrt{\bar{\Lambda}_1}}{\bar{\Lambda}_0}\left[\frac{\lambda_0+\mathrm{i}Y_{\xi,0}(\zeta_c)}{\mathcal{G}_0(\zeta_c)}\right]^{3/2}.\tag{A18}$$

In accordance with the above, in the representation of the variable ϱ, the singular point $\varrho=\varrho_c$ is located in the complex ϱ plane and satisfies the equation

$$\frac{\partial\Sigma(\tilde{k}_0,\varrho)}{\partial\tilde{k}_0}=0\quad\text{or}\quad\left[\tilde{k}_0^{(1)}(\varrho)-\tilde{k}_0^{(3)}(\varrho)\right]=0\,.\tag{A19}$$

Combining (A19) and (A14), one finds that ϱ_c satisfies the following equation:

$$\sigma_\mathrm{e}=\frac{2}{\sqrt{27}}\left(\frac{1-\mathrm{i}\varrho_c}{1+\mathrm{i}\varrho_c}\right)^{3/4}=\frac{\bar{\Lambda}_0}{\sqrt{\bar{\Lambda}_1}}\sigma_0.\tag{A20}$$

Three complex singular points can be obtained from (A20), their locations depend on the eigenvalue σ_0, as well as the parameters $\{\bar{\Lambda}_0, \bar{\Lambda}_1\}$. One of these singular points ϱ_c that we are interested in is located in the fourth quadrant of the complex ϱ plane.

As $\sigma_0 \to 0$, the singular point $\varrho_c \to -\mathrm{i}$. On the other hand, as σ_0 is a complex number with $|\sigma_0| = O(1)$ and $0 \leqslant \mathrm{Re}\{\sigma_0\} \ll 1$, one of the turning points ϱ_c that we are interested in is located in the fourth quadrant of the complex ϱ plane and away from the point $\varrho = -\mathrm{i}$.

C. First-order approximation of eigenvalue σ_1

We now turn to examine the asymptotic form of $F(\zeta)$ near $\zeta = \zeta_c$. For fixed σ_0, by making complete derivative with respect to ζ on both sides of (A13) we derive that

$$0 = \frac{\partial \Sigma}{\partial \bar{k}_0}\bar{k}_0'(\zeta) + \frac{\partial \Sigma}{\partial \zeta} = \left[\frac{F(\zeta)}{W\hat{\mathrm{P}}\mathrm{e}(1-\kappa)y_{*0}\mathcal{G}_0^2(\zeta)}\right]\bar{k}_0'(\zeta) + \frac{\partial \Sigma}{\partial \zeta}. \tag{A21}$$

On the other hand, by taking the partial derivative with respect to ζ of (A13), we derive

$$\begin{aligned}\frac{\partial \Sigma}{\partial \zeta} &= -\frac{\bar{k}_0}{\bar{\Lambda}_0\bar{\Lambda}_1\mathcal{G}_0^3}\left\{\frac{3\mathcal{G}_0'}{\mathcal{G}_0}\left[(\lambda_0 + \mathrm{i}Y_{\zeta,0})\bar{\Lambda}_1\mathcal{G}_0 - \bar{k}_0^2\right]\right.\\ &\quad \left. -\left[(\lambda_0 + \mathrm{i}Y_{\zeta,0})\bar{\Lambda}_1\mathcal{G}_0\right]'\right\}\\ &= \frac{\bar{k}_0}{\mathbb{M}W^2\hat{\mathrm{P}}\mathrm{e}(1-\kappa)y_{*0}\mathcal{G}_0^3(\zeta)}\left\{[(\lambda_0 + \mathrm{i}Y_{\zeta,0})\bar{\Lambda}_1\mathcal{G}_0]'\right.\\ &\quad \left. -\frac{3\mathcal{G}_0'}{\mathcal{G}_0}[(\lambda_0 + \mathrm{i}Y_{\zeta,0})\bar{\Lambda}_1\mathcal{G}_0 - \bar{k}_0^2]\right\}.\end{aligned} \tag{A22}$$

Finally, by combining the formula (A22) with (A21), we obtain

$$\begin{aligned}\frac{\bar{k}_0'(\zeta)}{\bar{k}_0(\zeta)} &= \frac{R_0(\zeta)}{F(\zeta)},\\ R_0(\zeta) &= \frac{1}{\mathbb{M}W\mathcal{G}_0(\xi)}\left\{\frac{3\mathcal{G}_0'}{\mathcal{G}_0}[(\lambda_0 + \mathrm{i}Y_{\xi,0})\bar{\Lambda}_1\mathcal{G}_0 - \bar{k}_0^2]\right.\\ &\quad \left. -[(\lambda_0 + \mathrm{i}Y_{\xi,0})\bar{\Lambda}_1\mathcal{G}_0]'\right\}.\end{aligned} \tag{A23}$$

From (A11), it is then derived that as $\zeta \to \zeta_c$, $F(\zeta_c)F'(\zeta_c) = O(1)$, or

$$F(\zeta) \propto (\zeta - \zeta_c)^{\frac{1}{2}}. \tag{A24}$$

Now, we rewrite (A10) in the following form:

$$\bar{k}_1(\xi) = \frac{R_1(\xi)}{F(\xi)} - \mathrm{i}\frac{R_2(\xi)}{F(\xi)}\frac{\bar{k}_0'(\xi)}{\bar{k}_0(\xi)}, \tag{A25}$$

where it is denoted that

$$\begin{aligned}R_1(\xi) &= \left\{ - W\hat{\mathrm{P}}\mathrm{e}[\lambda_{\mathrm{G}} - (1-\kappa)y_{*0})]Y_{\eta\eta}(\xi,0)\right.\\ &\quad \left. -\frac{\mathrm{i}\bar{k}_0^2}{\mathbb{M}W}\frac{\partial}{\partial \xi}\left[\frac{1}{\mathcal{G}_0(\xi)}\right] + \sigma_1 W\hat{\mathrm{P}}\mathrm{e}(1-\kappa)y_{*0}\mathcal{G}_0^2(\xi)\right\},\\ R_2(\xi) &= \frac{2\bar{k}_0^2}{\mathbb{M}W}\left[\frac{1}{\mathcal{G}_0(\xi)}\right].\end{aligned} \tag{A26}$$

It is clear from (A25) that the solution $\bar{k}_1(\zeta)$ has an isolated point singularity at ζ_c and as $\zeta \to \zeta_c$,

$$\bar{k}_1(\zeta) \sim \frac{m_1 R_1(\zeta_c)}{(\zeta - \zeta_c)^{\frac{1}{2}}} + \frac{m_2}{(\zeta - \zeta_c)} + O(1), \tag{A27}$$

where $m_1, m_2 = O(1)$. Note that the function $\bar{k}_1(\zeta)$ must be an analytic function in the complex ζ plane with some isolated singular points. Hence, it can be expanded into the Laurent series near the singular point ζ_c. In our case it implies from (A27) that

$$R_1(\zeta_c) = 0 \tag{A28}$$

must hold, and the point $\zeta = \zeta_c$ is actually a simple pole of the function $\bar{k}_1(\zeta)$ in the complex ζ plane. The condition (A28) yields

$$\begin{aligned}\sigma_1 &= \frac{1}{W\hat{\mathrm{P}}\mathrm{e}(1-\kappa)y_{*0}\mathcal{G}_0^2(\zeta_c)}\left\{W\hat{\mathrm{P}}\mathrm{e}\big[\lambda_{\mathrm{G}} - (1-\kappa)y_{*0}\big]\right.\\ &\quad \left. \times Y_{\eta\eta}(\zeta_c,0) - \frac{\mathrm{i}F_0(\zeta_c)\mathcal{G}_0'(\zeta_c)}{3\mathcal{G}_0(\zeta_c)}\right\}.\end{aligned} \tag{A29}$$

---

[1] J. W. Rutter and B. Chalmers, Can. J. Phys. **31**, 15 (1953).

[2] W. W. Mullins and R. F. Sekerka, J. Appl. Phys. **34**, 323 (1963).

[3] W. W. Mullins and R. F. Sekerka, J. Appl. Phys. **35**, 444 (1964).

[4] P. Pelcé and A. Pumir, J. Cryst. Growth **73**, 337 (1985).

[5] K. Somboonsuk, J. T. Mason, and R. Trivedi, Metall. Trans. A **15**, 967 (1984).

[6] T. Dombre and V. Haankim, Phys. Rev. A **36**, 2811 (1987).

[7] A. Karma, Phys. Rev. A **34**, 4353 (1986).

[8] A. Karma and P. Pelcé, Phys. Rev. A **39**, 4162 (1989).

[9] A. Karma and P. Pelcé, Phys. Rev. A **41**, 4507 (1990).

[10] A. Karma and P. Pelcé, Phys. Rev. A **41**, 6741 (1990).

[11] P. Kopczynski, W.-J. Rappel, and A. Karma, Phys. Rev. Lett. **77**, 3387 (1996).

[12] W. Losert, D. A. Stillman, H. Z. Cummins, P. Kopczynski, W.-J. Rappel, and A. Karma, Phys. Rev. E **58**, 7492 (1998).

[13] J. D. Weeks and W. van Saarloons, Phys. Rev. A **39**, 2772 (1989).

[14] M. Mashaal, M. Ben Amar, and V. Hakim, Phys. Rev. A **41**, 4421 (1990).

[15] J. D. Weeks, W. van Saarloons, and M. Grant, J. Cryst. Growth **112**, 244 (1991).

[16] S. H. Davis, J. Fluid Mech. **212**, 241 (1990).

[17] B. Caroli, C. Caroli, and B. Roulet, *Solids Far from Equilibrium* (Cambridge University Press, Cambridge, UK, 1991), p. 155.

[18] S. H. Davis, in *Handbook of Crystal Growth, Vol. 1: Fundamentals, Part B: Transport and Stability*, edited by D. T. J. Hurle (Elsevier, Amsterdam, 1993), p. 859.

[19] B. Billia and R. Trivedi, in *Handbook of Crystal Growth, Vol. 1: Fundamentals, Part B: Transport and Stability*, edited by D. T. J. Hurle (Elsevier, Amsterdam, 1993), p. 899.

[20] G.-L. Ding, W.-D. Huang, X. Lin, and Y.-K. Zhou, J. Cryst. Growth **177**, 281 (1997).

[21] L. H. Ungar and R. A. Brown, Phys. Rev. B **31**, 5931 (1985).

[22] R. Narayanan and R. A. Brown, Ph.D. Thesis, MIT, 1991.

[23] M. Georgelin and A. Pocheau, Phys. Rev. E **57**, 3189 (1998).

[24] A. Pocheau and M. Georgelin, J. Cryst. Growth **206**, 215 (1999).

[25] A. Pocheau and M. Georgelin, Phys. Rev. E **73**, 011604 (2006).

[26] M. Georgelin, S. Bodea, and A. Pocheau, Europhys. Lett. **77**, 46001 (2007).

[27] M. Georgelin and A. Pocheau, Phys. Rev. E **81**, 031601 (2009).

[28] J. Kageyama, Y. Sasajima, and M. Ichimura, Mater. Trans. **46**, 2003 (2005).

[29] S. Gurevich, M. Plapp, R. Trivedi, and A. Karma, Phys. Rev. E **81**, 011603 (2010).

[30] B. Echebarria, A. Karma, and S. Gurevich, Phys. Rev. E **81**, 021608 (2010).

[31] P. G. Saffman and G. I. Taylor, Proc. R. Soc. London A **245**, 312 (1958).

[32] J. Mclean and P. G. Saffman, J. Fluid Mech. **102**, 455 (1981).

[33] Y. Q. Chen and J. J. Xu, Phys. Rev. E **83**, 041601 (2011).

[34] J. J. Xu, European J. Appl. Math. **2**, 105 (1991).

[35] J. J. Xu, European J. Appl. Math. **7**, 169 (1996).

[36] J. J. Xu, IMA J. Appl. Math. **57**, 101 (1996).

[37] J. J. Xu, *Interfacial Wave Theory of Pattern Formation: Selection of Dendrite Growth and Viscous Fingering in a Hele-Shaw Flow* (Springer-Verlag, Berlin, 1998).

[38] J. J. Xu, Phys. Rev. A **43**, 930 (1991).

[39] J. J. Xu, Phys. Rev. E **53**, 5051 (1996).

[40] Y. Q. Chen, X. X. Tang, and J. J. Xu, Chinese Phys. B **18**, 671 (2009).

[41] Y. Q. Chen, X. X. Tang, and J. J. Xu, Chinese Phys. B **18**, 686 (2009).

[42] J. J. Xu and D. S. Yu, J. Cryst. Growth **226**, 378 (2001).

[43] J. C. LaCombe, M. B. Koss, Giummarra, J. E. Frei, Lupulecscu, and M. E. Glicksman, in *Coherent Structures in Comples System*, Lecture Notes in Physics, Vol. 567, edited by D. Reguera, L. L. Bonilla, and J. M. Rabi (Springer-Verlag, Berlin, 2001), p. 283.